

1 **Molecular Determinants of  $\mu$ -Conotoxin KIIIA Interaction with the**  
2 **Human Voltage-Gated Sodium Channel Nav1.7**

3

4

5 **Ian H. Kimball<sup>1,\*</sup>, Phuong T. Nguyen<sup>1,\*</sup>, Baldomero M. Olivera<sup>3</sup>,**

6 **Jon T. Sack<sup>1,2,‡</sup>, Vladimir Yarov-Yarovoy<sup>1,2,‡</sup>**

7

8 <sup>1</sup>Department of Physiology and Membrane Biology, UC Davis, Davis, CA, USA,

9 <sup>2</sup>[Department of Anesthesiology and Pain Medicine, UC Davis, Davis, CA, USA,](#)

10 <sup>3</sup>Department of Biology, University of Utah, Salt Lake City, UT, USA

11 \* - these authors contributed equally to this work

12 ‡ corresponding authors

## 13 **Abstract**

14 The voltage-gated sodium (Nav) channel subtype Nav1.7 plays a critical role in pain signaling,  
15 making it an important drug target. Here we studied the molecular interactions between  $\mu$ -  
16 conotoxin KIIIA (KIIIA) and the human Nav1.7 channel (hNav1.7). We developed a structural  
17 model of hNav1.7 using Rosetta computational modeling and performed in silico docking of KIIIA  
18 using RosettaDock to predict residues forming specific pairwise contacts between KIIIA and  
19 hNav1.7. We experimentally validated these contacts using mutant cycle analysis. Comparison  
20 between our KIIIA-hNav1.7 model and the cryo-EM structure of KIIIA-hNav1.2 revealed key  
21 similarities and differences between Nav channel subtypes with potential implications for the  
22 molecular mechanism of toxin block. [The accuracy of our integrative approach, combining](#)  
23 [structural data with computational modeling, experimental validation, and molecular dynamics](#)  
24 [simulations, suggests that Rosetta structural predictions will be useful for rational design of novel](#)  
25 [biologics targeting specific Nav channels.](#)

## 26 **Introduction**

27 Voltage-gated sodium (Nav) channels play a key role in the action potential generation in excitable  
28 cells (Hille, 2001; Catterall, 2014; Ahern et al., 2016). The nine subtypes of Nav channel  $\alpha$ -  
29 subunits (named Nav1.1-Nav1.9) are differentially expressed throughout tissues, and are targets  
30 of therapeutics for pain, cardiac arrhythmias, and epilepsy (Catterall et al., 2005). Human Nav1.7  
31 (hNav1.7) channel is important for pain signaling and its mutations have been linked to severe  
32 pain disorders ranging from complete lack of pain sensation to extreme sensitivity to pain (Dib-  
33 Hajj et al., 2013; Bennett et al., 2019; Dib-Hajj and Waxman, 2019). Clinical use of local anesthetic  
34 drugs, such as lidocaine, is limited because they bind to a highly conserved receptor site within the  
35 Nav channel pore lumen, and are consequently non-selective among human Nav subtypes  
36 (Ragsdale et al., 1994; Yarov-Yarovoy et al., 2001; Yarov-Yarovoy et al., 2002; Nguyen et al.,  
37 2019). [The receptor sites of other Nav blockers have nuanced differences between subtypes and](#)  
38 [molecular mechanisms of channel blockade that could enable rational design of Nav subtype-](#)  
39 [selective therapeutics \(Payandeh and Hackos, 2018\).](#)

40 The search for novel Nav channel modulators has identified small disulfide-knotted peptide toxins  
41 from cone snails (conotoxins) (Wilson et al., 2011), which target the extracellular vestibule of the  
42 Nav channel pore and offer useful peptide scaffolds for rational design of novel peptide-based  
43 therapeutics to potentially treat pain, arrhythmias, and epilepsy (French et al., 2010; Gilchrist et  
44 al., 2014).  $\mu$ -conotoxin KIIIA (KIIIA) is a 16 amino acid peptide that potently inhibits TTX-  
45 sensitive Nav channels (Zhang et al., 2007; Wilson et al., 2011; Khoo et al., 2012) (Figure 1A). [A](#)  
46 [pain assay in mice suggested that KIIIA potentially has analgesic properties \(Zhang et al., 2007\).](#)  
47 [Notably, a variant of saxitoxin that targets the same receptor site in hNav1.7 as KIIIA is now in a](#)  
48 [Phase I clinical trial for treatment of post-operative pain \(Mulcahy et al., 2019; Pajouhesh et al.,](#)

49 [2020; SiteOne Therapeutics, 2021](#)). KIIIA has variable degrees of affinity and block for the  
50 different Nav channel subtypes, with 5 nM affinity for rat Nav1.2, 37 nM for rat Nav1.4, and 97  
51 nM for hNav1.7 (Zhang et al., 2007; McArthur et al., 2011; Wilson et al., 2011). Structure-activity  
52 relationship studies have identified the KIIIA residues K7, W8, R10, D11, H12 and R14 as key for  
53 binding to various Nav channel subtypes (Zhang et al., 2007; McArthur et al., 2011). Specifically,  
54 K7, R10 and R14 have been shown to contribute to both binding affinity and block of hNav1.7  
55 (McArthur et al., 2011). Notably, the relative contribution of KIIIA residues in binding to Nav  
56 channels vary between channel subtypes. [For example, substitution R14A in KIIIA reduces the](#)  
57 [affinity for Nav1.2 and Nav1.4 by 740-fold and 180-fold, respectively, while reducing the affinity](#)  
58 [for Nav1.7 by only 5-fold \(McArthur et al., 2011\). Similarly, substitution R10A in KIIIA reduces](#)  
59 [the affinity for Nav1.2 and Nav1.4 by 32-fold and 27-fold, respectively, while reducing the affinity](#)  
60 [for Nav1.7 by only 14-fold \(McArthur et al., 2011\).](#) In addition, KIIIA blocks Nav channels  
61 incompletely and can co-bind with tetrodotoxin (TTX) to TTX-sensitive Nav channels (Zhang et  
62 al., 2009).

63 [A previous study identified the importance of Nav channel residues near the selectivity filter on](#)  
64 [the P2-helix in domain III \(DIII\) for their apparent coupling to residues R10 and R14 on KIIIA](#)  
65 [\(McArthur et al., 2011\). Notably, the P2-helix in DIII of hNav1.7 has threonine at position 1398](#)  
66 [and an isoleucine at position 1399, while all other human Nav channels have methionine and](#)  
67 [aspartate at the corresponding positions \(McArthur et al., 2011\). These residues were proposed to](#)  
68 [play an important role in the selectivity of KIIIA binding to Nav1.2 and Nav1.4 versus to Nav1.7](#)  
69 [\(McArthur et al., 2011\). Molecular modeling of KIIIA binding to rNav1.4 using restraints from](#)  
70 [experimental data suggested specific contacts between KIIIA and the P2-helix in DIII \(Korkosh et](#)



71 [al., 2014](#)). However, these studies did not provide an explanation for the significant effect of the  
72 KIIIA mutations H12A, W8A and D11A on toxin affinity.

73 In this study, we used computational and experimental approaches to investigate the molecular  
74 mechanism of the KIIIA interaction with hNav1.7. [We specifically focused on human Nav1.7 as](#)  
75 [a target due to its importance in pain signaling and our goal to rationally design novel KIIIA-based](#)  
76 [peptides targeting human Nav1.7 as potential therapeutics to treat chronic pain. We selected KIIIA](#)  
77 [among conotoxins identified to date because it has the highest potency for human Nav1.7](#) (Zhang  
78 et al., 2007; McArthur et al., 2011). We present a structural model of KIIIA binding to the hNav1.7  
79 channel based on the eukaryotic electric eel Nav1.4 cryo-EM structure (Yan et al., 2017). Our  
80 model revealed binding of KIIIA to hNav1.7 at the interface between the P2-helices in domain II  
81 (DII) and DIII, which exposed a partially open ion conduction pathway that may explain the  
82 incomplete blocking characteristic of the toxin. [While many KIIIA mutations have been previously](#)  
83 [characterized on Nav1.2 and Nav1.4 channels, only a limited number of KIIIA mutants had been](#)  
84 [tested on Nav1.7. We independently characterized many of the KIIIA mutations on Nav1.7 in our](#)  
85 [laboratory, to confirm previously published data and to validate affinities that serve as the basis of](#)  
86 [mutant cycle calculations. Our study for the first time tested effects of the following mutations:](#)  
87 [\(1\) KIIIA W8 and D11A on the wild-type hNav1.7; \(2\) hNav1.7 Y362C, E919Q, D923A with the](#)  
88 [wild-type KIIIA; \(3\) paired toxin—channel mutations K7A—E919Q, D11A—E919Q, and](#)  
89 [H12A—D923A.](#) We identified several unique contacts between KIIIA and extracellular loops on  
90 hNav1.7, providing key structural insights into binding specificity for different Nav channel  
91 subtypes. We used mutant cycle analysis to validate representative pairwise contacts between  
92 specific residues on KIIIA and hNav1.7 identified from our structural model of the KIIIA –  
93 hNav1.7 complex. Remarkably, the published cryo-EM structure of KIIIA - hNav1.2 complex (Pan

94 et al., 2019) agrees with findings from our computational modeling and functional study. The  
95 accuracy of peptide toxin – Nav channel interaction modeling suggests that Rosetta predictions are  
96 sufficiently precise for the rational design of novel selective peptide inhibitors targeting Nav  
97 channels with high selectivity and potency.

98

## 99 **Results**

100

### 101 **Molecular modeling suggests eccentric binding of KIIIA to DII and DIII of the hNav1.7 pore**

102 To characterize the molecular mechanism of the KIIIA interaction with hNav1.7, we utilized  
103 computational modeling and functional testing approaches as described below. When this study  
104 was conducted, the cryo-EM structure of the electric eel Nav1.4 (eeNav1.4) (Yan et al., 2017)  
105 channel was the closest structural homolog available to build a homology model of hNav1.7. The  
106 eeNav1.4 structure shares ~54% sequence identity with hNav1.7 overall and ~75% sequence  
107 identity over the hNav1.7 pore region. We used the RosettaCM modeling approach (Song et al.,  
108 2013; Bender et al., 2016) to generate a structural model of hNav1.7 based on the eeNav1.4  
109 structure (Yan et al., 2017) and the Rosetta protein-protein docking approach (Gray et al., 2003;  
110 Wang et al., 2007; Bender et al., 2016) to predict a structure of the KIIIA – hNav1.7 complex and  
111 identify specific residues forming interactions between KIIIA and hNav1.7 (see Materials and  
112 methods, and coordinates of our KIIIA – hNav1.7 model in Supplement File – Model 1). **Our**  
113 **model revealed an eccentric or off-center binding of KIIIA to hNav1.7, where the KIIIA helical**  
114 **region is positioned off the central axis of the selectivity filter with the positively charged KIIIA**  
115 **residues facing the P2-helices (Figure 1B). The position and orientation of KIIIA in our model is**  
116 **different from KIIIA binding to the P2-helix in DIII previously suggested by computational**

117 modeling (McArthur et al., 2011; Korkosh et al., 2014) and lanthanide-based resonance energy  
118 transfer (Kubota et al., 2017) studies. The KIIIA binding site just above the selectivity filter in our  
119 model is different from TTX and saxitoxin (STX) binding deeper into the selectivity filter region  
120 (Shen et al., 2018; Shen et al., 2019). Mapping of the open aqueous space surrounding the KIIIA  
121 - hNav1.7 binding interface revealed a tunnel traversing from the extracellular environment to the  
122 channel pore cavity (Figure 1C). The most constricted part of this aqueous tunnel is within the  
123 selectivity filter region, where the radius of the open aqueous space narrows to  $\sim 1$  Å. KIIIA bound  
124 to the upper region of the selectivity filter and constricted the open space to a minimum radius of  
125  $\sim 2.5$  Å, which is large enough to allow sodium ion conduction and consistent with the  
126 characteristic incomplete block of Nav channels by KIIIA (Zhang et al., 2007; McArthur et al.,  
127 2011). Notably, the cryoEM structure of KIIIA – hNav1.2 (Pan et al., 2019) reveals a binding pose  
128 similar to our model, as described later in this paper (Figure 4A).

129

### 130 **Pairwise interactions identified from the KIIIA - hNav1.7 complex model**

131 To identify key KIIIA residues at the toxin – channel interface, we first examined the contribution  
132 of KIIIA residues to the interaction with hNav1.7 using an *in silico* alanine scan. Non-cysteine  
133 residues on KIIIA were mutated to alanine and changes in Rosetta binding energy ( $\Delta\Delta G$ ) were  
134 reported in the arbitrary Rosetta Energy Units (R.E.U). Our analysis revealed the active surface of  
135 KIIIA with residues K7, W8, R10, H12, and R14 each having significant contribution to the  
136 binding energy (Figure 1D and E). K7, W8, R10, and H12 are located on the same face of KIIIA's  
137 alpha helix, while R14 is located within the C-terminal tail region of the toxin. Our KIIIA –  
138 hNav1.7 model predicts that positively charged residue K7 forms a salt bridge with E919 on the  
139 P2-helix in DII (we use hNav1.7 residue numbering throughout the manuscript unless otherwise

140 noted) (Figure 1F). In addition, W8 and H12 were shown to form hydrogen bonds with Y339 on  
141 the extracellular loop between S5 and the P1-helix (S5P1) in DI and D923 on the P2-helix in DII,  
142 respectively (Figure 1F). D11 is positioned near the interface between the P2-helices in DII and  
143 DIII and forms hydrogen bonds with both K7 on KIIIA and T1398 on the P2-helix in DIII (Figure  
144 1F). The other positively charged KIIIA residues, R10 and R14, interact with two negatively  
145 charged residues: D1662 on the extracellular loop S5P1 in DIV and E1417 on the extracellular  
146 loop between the P2-helix and S6 (P2S6) in DIII. Notably, R14 also interacts with Y1416 on the  
147 extracellular P2S6 loop in DIII and contributes to a cation- $\pi$  interaction tower formed by Y1402  
148 on the P2-helix in DIII, R896 on the extracellular loop S5P1 in DII, and Y1416 (Figure 1F). **The**  
149 **R10 of KIIIA is in proximity to I1399 on the P2-helix in DIII in agreement with the significant**  
150 **coupling energy between R10 and D1241 on the P2-helix in DIII in rNav1.4 reported previously**  
151 **(McArthur et al., 2011). While KIIIA N3 is near E307 in the extracellular loop S5P1 in DI, this**  
152 **interaction may not be substantial as shown by minimal change in Rosetta binding energy ( $\Delta\Delta G$ )**  
153 **from our *in silico* alanine scan (Figure 1D). N3 has been shown to be not critical for KIIIA**  
154 **interaction with rNav1.2 and rNav1.4 channels (Zhang et al., 2007).**

155

## 156 **Functional mapping of KIIIA residues at the toxin – channel interface supports the predicted** 157 **KIIIA – hNav1.7 model**

158 To test the accuracy of our KIIIA – hNav1.7 model, we first confirmed the activity of the wild-  
159 type KIIIA on the wild-type hNav1.7 using whole-cell voltage-clamp recordings. **To estimate the**  
160 **KIIIA binding affinity, we performed concentration-response experiments and obtained an  $IC_{50}$  of**  
161  **$410\pm 160$  nM when fit to a Hill equation assuming a single binding site (Figure 2). This fitting**  
162 **suggested a maximal block of  $95\pm 3.3\%$  of total current in agreement with previous studies**

163 concluding that Nav channels retain 5-10% of their conductance when blocked by KIIIA (Zhang  
164 et al., 2007; McArthur et al., 2011). The WT-KIIIA first order association rate ( $k_{on}$ ) was determined  
165 based on single exponential fits to the kinetics of block after toxin addition (Table 1, see Materials  
166 and Methods equation 3). The extremely slow dissociation of the wild-type KIIIA from hNav1.7  
167 complicated accurate determination of dissociation kinetics, as less than 10% recovery was  
168 observed during wash-off experiments lasting up to ~30 min. Constraining single exponential fits  
169 of the dissociation data to assume current recovers to initial levels, we obtained  $k_{off}$  of  $0.003 \text{ min}^{-1}$   
170 and a  $K_d$  of 59 nM, which is close to the previously reported  $K_d$  of 97 nM (McArthur et al., 2011).  
171 Temperature differences between our experiments (~21°C) and the prior study (~25°C) might be  
172 responsible for differences in kinetics and affinities.

173 We performed an alanine scan of KIIIA residues that are positioned at the interface with hNav1.7  
174 in our model to determine their effect on binding affinity to the wild-type channel. As with WT-  
175 KIIIA,  $k_{on}$ ,  $k_{off}$ , and  $K_d$  were determined from single exponential fits of peak current during  
176 depolarizing voltage steps and are summarized in Table 1; representative data are shown in Figure  
177 2—figure supplement 1A. In the absence of Hill fits of concentration response curves for KIIIA  
178 variants,  $k_{on}$  was calculated according to equation 2 (see Materials and Methods). KIIIA  
179 substitutions K7A and H12A both had nearly 100-fold decreases in affinity for the wild-type  
180 hNav1.7 channel, in agreement with previously published data (Zhang et al., 2007; Zhang et al.,  
181 2009; McArthur et al., 2011). We found that KIIIA substitutions W8A and D11A had a 50- and  
182 10-fold reduction in affinity for the wild-type hNav1.7 channel, respectively (Figure 2D). The  
183 KIIIA point mutations had little effect on the association rate relative to wild-type KIIIA, with  
184 D11A showing the largest effect at a 3-fold increase in association rate (Figure 2D). The observed  
185 change in affinity from neutralizing mutations of charged residues was largely driven by 36-fold

186 to 116-fold increases in toxin dissociation rates (Figure 2D). The KIIIA-D11A substitution resulted  
187 in both an increase in  $k_{on}$  and  $k_{off}$ . This substitution also would eliminate contact with Nav1.7-  
188 specific T1398 on the P2-helix in DIII observed in our model. Prior studies had observed that the  
189 D11A substitution had no effect on dissociation from rNav1.2, but had a small effect on rNav1.4  
190 binding—slowing  $k_{off}$  4-fold and very little effect on  $k_{on}$  (Zhang et al., 2007). The reductions in  
191 KIIIA affinity from alanine mutations seen *in vitro* correspond to key residues forming the KIIIA-  
192 hNav1.7 interface observed in our model (Figure 1B).

193 We estimated maximal block from fractional current remaining at sub-saturating concentrations  
194 of toxin variants by assuming a single binding site with  $K_d = k_{off} / k_{on}$  and extrapolating to maximal  
195 block (see Materials and Methods equations 2, 5, and 7). We caution that these estimates of  
196 maximal block are model-dependent and of limited precision, and not as definitive as single  
197 channel measurements or experiments in saturating doses of toxin would be. Bearing these  
198 cautions in mind, we note that alanine substitution at position 7 (Figure 2C, Table 1) reduces  
199 maximal block to  $74 \pm 4.9\%$ , while substitutions at positions 8 and 11 did not detectably reduce  
200 maximal block ( $90 \pm 9.4\%$ , and  $100 \pm 1.2\%$ , respectively) (Table 1). In addition to levels of block  
201 previously reported for K7A, H12A, R10A, R14A variants (McArthur et al., 2011), these results  
202 are consistent with an orientation placing K7 towards the acidic residues of the selectivity filter  
203 (Figure 1F).

204

## 205 **Table 1**

### 206 **Block of hNav1.7 by KIII variants**

207 Fractional block at saturating concentrations determined from extrapolation from kinetic data.

<i>Channel and Toxin (n)</i>	$k_{on}$ ( $\mu\text{M}^{-1}\text{min}^{-1}$ )	<i>SEM</i>	$k_{off}$ ( $\text{min}^{-1}$ )	<i>SEM</i>	$K_d$ ( $\mu\text{M}$ )	<i>SEM</i>	$F_{block}$	<i>SEM</i>
<i>WT-hNav1.7 x WT-KIIIA (5)</i>	0.054	0.011	0.003	0.001	0.059	0.007	0.95 <sup>a</sup>	0.033
<i>WT-hNav1.7 x KIIIA-K7A (5)</i>	0.064	0.018	0.274	0.012	4.291	1.507	0.74	0.049
<i>WT-hNav1.7 x KIIIA-W8A (3)</i>	0.110	0.045	0.329	0.097	2.990	1.719	0.90	0.094
<i>WT-hNav1.7 x KIIIA-D11A (4)</i>	0.164	0.014	0.109	0.008	0.663	0.056	1.00	0.012
<i>WT-hNav1.7 x KIIIA-H12A (5)</i>	0.047	0.027	0.349	0.240	7.405	2.801	0.88 <sup>b</sup>	0.019

208 *a* – Fractional block was determined from the Hill fit of concentration-response data (Figure 2B).

209 *b* – Fractional block reported by McArthur, et al., 2011. This value was used to constrain kinetic parameter estimates  
210 from association experiments.

211 *n* – number of cells tested.

212

## 213 **Functional mapping of hNav1.7 residues at the toxin – channel interface support KIIIA** 214 **binding to the P2-helices in DI and DII**

215 To test the accuracy of the orientation of KIIIA in our model, we used mutations in the P2-helices  
216 of DI and DII in the outer pore (Figure 1). We mutated the hNav1.7 N365 and Y362 residues on  
217 the P2-helix in DI and E919 and D923 on the P2-helix in DII (Figure 1F). N365A slowed  
218 dissociation such that  $k_{off}$  was not measurable during the course of our wash-out experiments,  
219 precluding measurement of affinity, but suggesting a limited contribution to toxin binding of this  
220 position (Figure 2–Supplement 1, Table 2). Y362C however, produced a modest increase in both  
221 association and dissociation yielding a 7.5-fold reduction in affinity corresponding to 1.2  
222 kcal•mol<sup>-1</sup> (Figure 2E). The E919A mutation did not produce measurable current, yet the E919Q  
223 mutation produced functional currents and reduced binding of the wild-type KIIIA by 42-fold

224 corresponding to a 2.2 kcal•mol<sup>-1</sup> reduction in affinity (Figure 2E). Our model shows a salt bridge  
 225 between E919 and toxin residue K7 (Figure 1F); the effect of this charge neutralization  
 226 demonstrates the importance of an acidic residue at this position for toxin binding. The lack of  
 227 current in the E919A mutant points to a potential steric contribution of this location for pore  
 228 stability given the proximity to the selectivity filter (Figure 1C, 1F), or poor expression. Our model  
 229 also shows a hydrogen bond between toxin residue H12 and D923, one helix turn up the DII-P2  
 230 helix from E919 (Figure 1F). The substitution D923A likewise reduced affinity of the wild-type  
 231 KIIIA by 40-fold, or 2.2 kcal•mol<sup>-1</sup> (Figure 2E) suggesting the elimination of such an interaction.  
 232 Overall, hNav1.7 mutations Y362C, E919Q, and D923A reduced the binding of the wild-type  
 233 KIIIA to hNav1.7 in agreement with our structural model of the KIIIA – hNav1.7 complex and  
 234 published KIIIA – hNav1.2 structure (Pan et al., 2019). The effects of mutations E919Q and  
 235 D923A in the P2-helix in DII are consistent with the toxin – channel protein-protein interface  
 236 suggested by our model (see representative data in Figure 2—figure supplement 1B). Overall, our  
 237 KIIIA alanine scan experiments support the toxin – channel protein-protein interface observed in  
 238 our KIIIA – hNav1.7 model and the published KIIIA - Nav1.2 structure (Pan et al., 2019).

## 239 **Table 2**

### 240 **Block of hNav1.7 mutants by KIIIA**

241 Fractional block at saturating concentrations determined from extrapolation from kinetic data.

<i>Channel and Toxin (n)</i>	<i>k<sub>on</sub></i> (μM <sup>-1</sup> min <sup>-1</sup> )	<i>SEM</i>	<i>k<sub>off</sub></i> (min <sup>-1</sup> )	<i>SEM</i>	<i>K<sub>d</sub></i> (μM)	<i>SEM</i>	<i>F<sub>block</sub></i> <sup>a</sup>	<i>SEM</i>
<i>WT-hNav1.7 x WT-KIIIA (5)</i>	0.054	0.011	0.003	0.001	0.059	0.007	0.95 <sup>a</sup>	0.033
<i>Y362C x WT-KIIIA (3)</i>	0.101	0.016	0.044	0.004	0.436	0.052	0.75	0.055



<i>N356A x WT-KIIIA</i> (2)	0.102	0.010	n.d. <sup>b</sup>	-	n.d.	-	0.80	0.004
<i>E919Q x WT-KIIIA</i> (3)	0.040	0.003	0.101	0.003	2.51	0.16	0.92	0.028
<i>D923A x WT-KIIIA</i> (3)	0.083	0.022	0.193	0.022	2.34	0.41	0.89	0.037

242 *a* – Fractional block was determined from the Hill fit of concentration-response data (Figure 2B)

243 *b* – No dissociation was observed during washout,  $F_{Block}$  is observed block.

244 *n* – number of cells tested.

245

## 246 **Double Mutant Cycle Analysis confirms pairwise interactions between KIIIA and hNav1.7-**

### 247 **DII**

248 Our alanine scan and previous studies have demonstrated the importance of several toxin and  
 249 channel residues for the binding of KIIIA to hNav1.7. To further validate specific pairwise toxin  
 250 – channel contacts predicted by our KIIIA – hNav1.7 model, we performed double-mutant cycle  
 251 analysis experiments (Hidalgo and MacKinnon, 1995; Schreiber and Fersht, 1995; Ranganathan  
 252 et al., 1996) assessing the contributions of specific pairwise contacts to the binding energy between  
 253 KIIIA and hNav1.7 (Figure 3). Specifically, we compared the effects of single and double  
 254 mutations at KIIIA positions K7 and D11 with hNav1.7 E919Q, and KIIIA H12 with Nav1.7  
 255 D923A (Figure 3A and Figure 3—figure supplement 1). Pairwise contacts can be identified on the  
 256 basis of the path-independence from the wild-type condition to the double-mutant condition: the  
 257 reduction in binding energy resulting from a mutation to either side of an interacting pair should  
 258 be non-additive in the double-mutant condition (Hidalgo and MacKinnon, 1995; Ranganathan et  
 259 al., 1996). Residue pairs that exhibit energetically additive effects of the double-mutant relative to  
 260 the single mutants do not make functional interactions contributing to the binding energy. These  
 261 effects are quantified by calculating the coupling coefficient  $\Omega$  (Materials and Methods Equation  
 262 8), and the coupling energy  $E_{coupling} = -RT\ln\Omega$  (Materials and Methods, Equation 9). Coupling

263 coefficient values differing from 1 indicate higher degrees of coupling, and  $E_{\text{coupling}} > 0.89$   
264 kcal·mol<sup>-1</sup> correlating with a close-contact interaction between the native sidechains (<4 Å)  
265 (Hidalgo and MacKinnon, 1995; Schreiber and Fersht, 1995; Ranganathan et al., 1996).  
266 Importantly, while directly interacting pairs are expected to show coupling, coupling can also  
267 result from allosteric effects. We tested the following pairs of double mutants: E919Q x K7A,  
268 D923A x H12A (Figure 3—figure supplement 1), which both interact directly in our model (Figure  
269 4A), and E919Q x D11A, which do not interact directly in our model, with the hypothesis that  
270 only the interacting pairs will exhibit  $E_{\text{coupling}} > 0.89$  kcal·mol<sup>-1</sup>. E919Q x D11A greatly reduced the  
271 toxin affinity ( $K_d = 14.2 \pm 5.8$  μM) relative to either of the single mutations, E919Q and D11A  
272 ( $2.34 \pm 0.16$  μM and  $0.66 \pm 0.06$  μM, respectively) (Figure 3B and Table 3), with  $\Omega = 0.5$  and  
273  $E_{\text{coupling}} = 0.40 \pm 0.009$  kcal·mol<sup>-1</sup>, values that do not support a direct interaction, consistent with the  
274 separation of these residues in our model (Table 4) (Schreiber and Fersht, 1995; Ranganathan et  
275 al., 1996). In contrast, the mutations E919Q and K7A, had no greater effect on binding affinity  
276 together ( $2.47 \pm 1.32$  μM) than either channel mutation E919Q ( $2.51 \pm 0.16$  μM), or the K7A variant  
277 alone ( $4.29 \pm 1.51$  μM) (Figure 3A and Table 3) and are indistinguishable from each other within  
278 error, indicating that mutation to either side eliminates an interaction with  $\Omega = 0.014$  and  
279  $E_{\text{coupling}} = 2.51 \pm 0.032$  kcal·mol<sup>-1</sup> (Table 4). Likewise, the D923A mutation reduced the affinity of  
280 WT-K111A ( $2.34 \pm 0.41$  μM), but was indistinguishable from that seen with both mutations D923A  
281 and H12A present ( $2.40 \pm 1.45$  μM) (Figure 3A and Table 3). The non-additive effect of these  
282 substitutions correlates with close contact between these residues that is eliminated upon mutation  
283 of either side  $\Omega = 0.008$  and  $E_{\text{coupling}} = 2.81 \pm 0.29$  kcal·mol<sup>-1</sup> (Table 4). The coupling energies  
284 observed between these pairs are consistent with pairwise interactions between charged amino  
285 acids (Hidalgo and MacKinnon, 1995; Schreiber and Fersht, 1995; Ranganathan et al., 1996).

286 These results are consistent with E919 – K7 and D923 – H12 pairwise interactions observed in  
 287 both our model (Figure 4A) and the recent structure of KIIIA - Nav1.2 complex (Pan et al., 2019),  
 288 which both show strong electrostatic interactions between these residue pairs, providing further  
 289 experimental validation of the KIIIA binding pose observed in our model.

290 **Table 3**

291 **Block of double-mutant cycle pairs of hNav1.7 and KIIIA**

<i>Channel and Toxin (n)</i>	$k_{on}$ ( $\mu\text{M}^{-1}\text{min}^{-1}$ )	<i>SEM</i>	$k_{off}$ ( $\text{min}^{-1}$ )	<i>SEM</i>	$K_d$ ( $\mu\text{M}$ )	<i>SEM</i>	$F_{block}$	<i>SEM</i>
<i>WT-hNav1.7 x WT-KIIIA (5)</i>	0.054	0.011	0.003	0.001	0.059	0.007	0.95 <sup>a</sup>	0.033
<i>WT-hNav1.7 x KIIIA-K7A (5)</i>	0.064	0.018	0.274	0.012	4.29	1.51	0.74	0.049
<i>WT-hNav1.7 x KIIIA-D11A (4)</i>	0.164	0.014	0.109	0.008	0.66	0.056	1.00	0.012
<i>WT-hNav1.7 x KIIIA-H12A (5)</i>	0.047	0.027	0.349	0.240	7.40	2.80	0.88 <sup>b</sup>	0.019
<i>E919Q x WT-KIIIA (3)</i>	0.040	0.003	0.101	0.003	2.51	0.16	0.92	0.028
<i>E919Q x KIIIA-K7A (3)</i>	0.044	0.015	0.108	0.021	2.47	1.32	0.48	0.066
<i>E919Q x KIIIA-D11A (3)</i>	0.124	0.046	1.790	0.369	14.2	5.79	0.92 <sup>c</sup>	0.028
<i>D923A x WT-KIIIA (3)</i>	0.083	0.022	0.193	0.022	2.34	0.41	0.89	0.037
<i>D923A x KIIIA-H12A (2)</i>	0.183	0.065	0.440	0.098	2.40	1.45	0.49	0.092

292 *a* – Fractional block was determined from the Hill fit of concentration-response data (Figure 2B).

293 *b* – Fractional block reported by McArthur, et al., 2011 was used to constrain kinetic parameter estimates from  
 294 association experiments.

295 *c* – Fractional block from E919Q mutation assumed to be the same as WT-KIIIA given lack of effect by KIIIA-D11A.

296 *n* – number of cells tested.

297

298 **Table 4**

299 **Coupling coefficients and coupling energies from double-mutant cycle experiments**

	<i>D923A x H12A</i>	<i>sd</i>	<i>E919Q x K7A</i>	<i>sd</i>	<i>E919Q x D11A</i>	<i>sd</i>
<i>E<sub>coupling</sub> kcal·mol<sup>-1</sup></i>	2.81	0.29	2.51	0.032	0.40	0.009
<i>1/Ω</i>	122	76.8	74.0	4.17	1.99	0.030

300 *Error calculated by linear propagation of uncertainty (Ku, 1966; Hidalgo and MacKinnon, 1995).*

301

302 **Nav channel isoforms with distinct toxin affinities have divergent residues at the KIIIA**  
303 **binding interface**

304 The differences in KIIIA binding affinity between the Nav channel isoforms likely arise from  
305 variations in sequence in the P2 helices and extracellular loop regions (Figure 4A and B). The  
306 published structure of the KIIIA - hNav1.2 complex (Pan et al., 2019) was not available when we  
307 generated our structural model of the KIIIA - hNav1.7 complex, yet it is consistent with our  
308 structural model and further supports this observation. The backbone root mean square deviation  
309 (RMSD) of the KIIIA - hNav1.7 model and the KIIIA - hNav1.2 structure over KIIIA and the P2-  
310 helices is ~1.0 Å (Figure 1—figure supplement 1B). The specific pairwise contacts between K7-  
311 E919 and H12-D923 in our KIIIA - hNav1.7 model, validated by our mutant cycle analysis, are in  
312 agreement with the corresponding pairwise contacts between K7-E945 and H12-D949 observed  
313 in the KIIIA - hNav1.2 complex structure (Figure 4A and B) (Pan et al., 2019). Our KIIIA -  
314 hNav1.7 model also predicted other contacts observed in the published KIIIA - hNav1.2 structure

315 (Pan et al., 2019), including pairwise interactions between KIIIA N3 and W8 with E307 and Y339,  
316 respectively, on the extracellular S5-P1 loop in DI (Figure 4A and B).

317

318 The KIIIA critical residues D11 and R10 in our KIIIA - hNav1.7 model are positioned similarly  
319 in the KIIIA - hNav1.2 structure, but details of toxin – channel interactions involving these residues  
320 are different (Figure 4A). D11 forms a hydrogen bond with T1398 on the P2-helix in DIII in our  
321 KIIIA - hNav1.7 model (Figure 4A), but the substitution of Thr (T1398) hNav1.7 to Met (M1425)  
322 on the P2-helix in DIII in hNav1.2 removes this interaction, and a new hydrogen bond is formed  
323 between D11 with the nearby residue Y1429 (Figure 4—figure supplement 1) (Pan et al., 2019).  
324 In the hNav1.2 structure, R10 interacts with D1426 on the P2-helix in DII, but the corresponding  
325 position in hNav1.7 is I1399, eliminating possible charge interaction with this residue in hNav1.7  
326 (Figure 4A and B). This difference potentially contributes to the R10 interaction with the nearby  
327 acidic residue D1662 on the extracellular S5-P1 loop in DIV of hNav1.7 (Figure 4—figure  
328 supplement 1). It is noticeable that Asp at position 1662 is unique to hNav1.7 - corresponding  
329 residues at this position in other Nav channel subtypes are Val, Ala, and Ser (Figure 4B).  
330 Additionally, the corresponding residues to T1398 and I1399 on the P2-helix in DIII of hNav1.7  
331 are Met and Asp, respectively, in all other human Nav channels. Because of that, it seems  
332 reasonable to hypothesize that these residues provide a major contribution to structural determinant  
333 of KIIIA interaction with hNav1.7.

334

335 The R14 residue on KIIIA is important for KIIIA binding to Nav channels and the substitution of  
336 Arginine to Alanine at this position has been shown to gain selectivity for hNav1.7 versus hNav1.2  
337 (McArthur et al., 2011). Both our KIIIA - hNav1.7 model and the KIIIA - hNav1.2 structure show

338 the positively charged R14 forming cation –  $\pi$  interactions with Y1416 (hNav1.7) or Y1443  
339 (hNav1.2) on the extracellular P2-S6 loop in DIII (Figure 4A). Notably, in the KIIIA - hNav1.2  
340 structure R14 is also in proximity to the negatively charged E919 (hNav1.2 numbering) on the  
341 extracellular S5-P1 loop in DII (Pan et al., 2019). However, in our KIIIA - hNav1.7 model, R14  
342 is in proximity to T893 on the extracellular S5-P1 loop in DII (which is corresponding to E919 in  
343 hNav1.2) and E1417 on the extracellular P2-S6 loop in DIII (Figure 4A and B). We reason that  
344 these differences may contribute to the reported selectivity of KIIIA R14A substitution against  
345 hNav1.7.

346  
347 Overall, despite the similarity in binding pose and channel architecture, sequence variance at KIIIA  
348 binding site, comprised of the P2 helices and extracellular loop regions likely contribute to  
349 differences in KIIIA binding affinity of between hNav1.7 and hNav1.2, and perhaps also among  
350 other channel isoforms.

351  
352 **Structural dynamics of KIIIA binding to hNav1.7 and hNav1.2 revealed by molecular**  
353 **dynamics simulations**

354 To further study the molecular mechanism of the KIIIA interaction with hNav1.7, we performed  
355 molecular dynamics (MD) simulations of our KIIIA - hNav1.7 complex model. The 3 independent  
356 1.5  $\mu$ s MD simulations revealed highly dynamic KIIIA binding with the backbone RMSDs  
357 between KIIIA and hNav1.7 interface fluctuating between 3.5 – 4.5 Å (Figure 5 – figure  
358 supplement 1). Remarkably, we observed key positively charged residues K7 and R10 on KIIIA  
359 interacted not only with the acidic residue on the P2-helix in DII identified from our model (E919

360 and D923) but also with acidic residues on the P2-helix in DIV. The density projection of these  
361 residues on the membrane plane revealed the primary amine group of K7 was mostly localized  
362 near D923 and E919 on P2-helix in DII and D1690 on P2-helix in DIV (see sites A1, A2 and A3  
363 in Figure 5A) while R10 was localized near E919 (DII) and D1690 (DIV) (Figure 5 – figure  
364 supplement 2). The dynamic interactions of K7 with multiple acidic residues on P2 helices is  
365 consistent with our functional characterization of KIIIA - hNav1.7 interactions where we observed  
366 a 100-fold reduction in  $K_d$  for the K7A mutation on KIIIA and only a 42-fold reduction for E919Q  
367 mutation on the channel. As an indication of highly dynamic interactions of KIIIA with hNav1.7,  
368 we also observed key residues on KIIIA formed interactions with multiple residues on the channel  
369 as shown in the fractional contact map (Figure 5). Notably, W8 frequently formed contacts with  
370 K310 and Y339 on the extracellular S5-P1 loop in DI. H12 interacted mainly with D923 on the  
371 P2-helix in DII and also with the backbone of P895 on the extracellular S5-P1 loop in DII. D11 is  
372 positioned deep at the interface between DII and DIII within a region formed by hNav1.7 residues  
373 R911 on the P1-helix in DII, E919 on the P2-helix in DII, and Y1402 on the P2-helix in DIII. R14  
374 primarily interacted with Y1416 on the extracellular P2-S6 loop in DIII, and T893, L894, P895  
375 and R896 on the extracellular loop in DII and did not maintain interaction with E1417 on the  
376 extracellular loop in DIII as initially identified in our model (Figure 5—figure supplement 2). In  
377 addition, during equilibration we consistently observed the initial placed sodium ion in the  
378 selectivity filter localized near E916 and E919 on the P1-P2-helix region in DII (Figure 5A – figure  
379 supplement 1), which agrees with the density identified as a sodium ion at the same position in the  
380 structure of the KIIIA - hNav1.2 complex (Pan et al., 2019). This sodium ion quickly diffused out  
381 to the extracellular bulk via an open passage formed between KIIIA and the selectivity filter region  
382 of the channel. The sodium ion escape is consistent with the incomplete block of Nav current

383 observed in experiments (Figure 2) and incomplete reduction of the unitary Nav channel  
384 conductance when KIIIA is bound (Zhang et al., 2007; McArthur et al., 2011).

385

386 We used the cryoEM structure of KIIIA - hNav1.2 complex (Pan et al., 2019) to study structural  
387 dynamics at the toxin – channel interface and compare them to dynamics observed in our KIIIA -  
388 hNav1.7 complex model (Figure 5A). We conducted 3 independent 1  $\mu$ s MD simulations using  
389 the same procedure as applied for the KIIIA - hNav1.7 model (see Materials and Methods). Similar  
390 to the simulations of our KIIIA – hNav1.7 model, the KIIIA - hNav1.2 complex structure was  
391 dynamic during simulations with the RMSDs at the toxin – channel interface between 3 - 5 Å  
392 (Figure 5 – supplement 1). We also observed that key positively charged residues K7 and R10 on  
393 KIIIA interacted with multiple acidic residues on the P2 helices of DI, DII, and DIV on hNav1.2  
394 (Figure 5B). The primary amine group of K7 was mainly localized near E945 and D949 on the P2-  
395 helix in DII and D1426 on the P2-helix in DIII (see sites B1, B2 and B3 in Figure 5B). Interactions  
396 with the conserved acidic residues D1717 on the P2-helix in DIV (corresponding to D923 and  
397 D1690 in hNav1.7, respectively) were more limited compared to that in the simulations of KIIIA  
398 - hNav1.7 model (see site A3 in Figure 5A). Similarly, R10 was localized near E945 on the P2-  
399 helix in DII and D1426 on the P2-helix in DIII while interactions with the conserved acidic residue  
400 D1717 (D1690 in hNav1.7) were less dominant compare to that in hNav1.7 (Figure 5 – figure  
401 supplement 1). These differences between hNav1.2 and hNav1.7 can be explained by a  
402 contribution of a single residue substitution in P2-helix in DIII. Particularly, D1426 on the P2-  
403 helix in DIII of hNav1.2 is conserved among all human Nav channel isoforms, except for hNav1.7,  
404 which has I1399 at this position (Figure 4). The absence of an acidic residue, Asp at the 1399  
405 position in hNav1.7 (D1426 in hNav1.2), substituted by a hydrophobic residue, I1399 may



406 facilitate interactions of positively charged K7 and R10 with the nearby acidic residue D1690 on  
407 the P2-helix in DIV in hNav1.7 (Figure 5—figure supplement 1). Indeed, functional studies  
408 showed that the mutation R10A produced a 35% reduction in KIIIA block of rNav1.4, while the  
409 loss of toxin block caused by the R10A mutation was largely rescued by hNav1.7-like Ile on the  
410 P2-helix in DIII (McArthur et al., 2011). Based on these observations, we speculate that dynamic  
411 interactions of basic residues K7 and R10 on KIIIA with acidic residues on P2-helix on hNav  
412 channels, driven by sequence variability at toxin – channel interface may provide a structural basis  
413 for differences in KIIIA interactions among hNav channel isoforms. The sodium ion in the KIIIA  
414 - hNav1.2 structure at the site formed by E942 and E945 (corresponding to E916 and E919 in  
415 hNav1.7) on the P1-P2-helix region in DII of hNav1.2 quickly diffused out to the extracellular  
416 bulk, in agreement with an incomplete block by KIIIA (Zhang et al., 2007) and our simulation of  
417 the KIIIA - hNav1.7 model (Figure 5A and B). We did not observe re-entering events of sodium  
418 ions into the hNav1.2 selectivity filter, similarly to our simulations of the KIIIA - hNav1.7 model.

419

## 420 **Discussion**

### 421 **Computational modeling and functional testing reveal molecular determinants of $\mu$ -** 422 **conotoxin KIIIA interaction with Nav1.7**

423 Our computational model of hNav1.7, docking of KIIIA to the hNav1.7 model, and functional  
424 testing of KIIIA and hNav1.7 mutations presented here were completed prior to the publication of  
425 KIIIA - hNav1.2 complex structure (Pan et al., 2019). While hNav1.7 and hNav1.2 channels share  
426 sequence homology within most of the KIIIA binding region, they exhibit several key differences  
427 at the toxin - channel interface. We functionally characterized specific pairwise contacts between

428 KIIIA and hNav1.7 predicted by our model, particularly between K7 on KIIIA and E919 on the  
429 P2-helix in DII and also between H12 on KIIIA and D923 on the P2-helix in DII. These pairwise  
430 interactions agree with the corresponding pairwise interactions between K7-E945 and H12-D949  
431 observed in the KIIIA - hNav1.2 complex structure (Figure 4A and B) (32). Interestingly, we also  
432 observed that our KIIIA – hNav1.7 complex model based on the eeNav1.4 structure is similar to  
433 our earlier KIIIA – hNav1.7 complex model based on the bacterial NavAb channel structure using  
434 experimental restraints (PDB: 3RVY (Payandeh et al., 2011)). In this effort, the pairwise distance  
435 constraints from available experimental data were used to model the interactions of GIIIA toxin, a  
436 close homolog of KIIIA with the homology model of hNav1.4 based on the bacterial NavAb  
437 structure. The model GIIIA – hNav1.4 were then subsequently used to build the KIIIA – hNav1.7  
438 model. It predicted accurately the KIIIA orientation and both the interaction of K7 with E919 and  
439 H12 with D923 (Figure 1—figure supplement 1A). However, the NavAb based model failed to  
440 identify the pairwise interaction of W8 and Y339 (interacted with E926 instead). This likely due  
441 to the limitation of the bacterial template with the difference in pore architecture compared to  
442 mammalian Nav channels and the absence of extracellular loop regions in the NavAb based model.  
443 Together, our work has demonstrated the predictive power of structural modeling with different  
444 degrees of experimental restraints to study peptide toxin – channel interactions.

445  
446 The Cryo-EM structures of hNav1.2, hNav1.4, rNav1.5, and hNav1.7 channels (Pan et al., 2018;  
447 Pan et al., 2019; Shen et al., 2019; Jiang et al., 2020) revealed that the extracellular vestibule of  
448 the channel pore targeted by KIIIA is surrounded by several relatively long loop regions, raising  
449 the possibility that the access pathway to the KIIIA binding site is relatively narrow. Restricted  
450 access and escape pathways for KIIIA binding could confer the relatively slow  $k_{on}$  and  $k_{off}$  rates

451 observed in our functional studies (Figures 2 and 3) and previously published data (Zhang et al.,  
452 2007; McArthur et al., 2011; Wilson et al., 2011). We speculate that variability in the Nav channel  
453 extracellular vestibule loops could underlie the differences in KIIIA kinetics.

454

455 While our KIIIA - hNav1.7 model and the published KIIIA - hNav1.2 structure are supported by  
456 functional data, further interactions of key charged residues K7 and R10 on KIIIA with multiple  
457 acidic residues on the channels was observed in our MD simulations and could provide insight  
458 into selectivity of the toxin and channel block. Notably, the unique residue I1399 on the P2-helix  
459 in DIII of hNav1.7 may contribute to KIIIA binding on hNav1.7 by influencing the interactions of  
460 K7 and R10 on KIIIA with acidic residues on the channel. We also observed escapes of sodium  
461 ions initially located in the selectivity filter in both KIIIA - hNav1.7 and KIIIA - hNav1.2 which  
462 agrees with functional data showing that KIIIA incompletely blocks Nav channels. Interestingly,  
463 despite having 150 mM of NaCl in the bulk solvent, we did not observe re-entering events of  
464 sodium ions in the selectivity filter during the 3 independent 1.5  $\mu$ s MD simulations. This possibly  
465 can be explained by the relatively high percentage (> 94%) of KIIIA block observed in both  
466 hNav1.7 and hNav1.2, which implied such re-binding events are rare and may not be observed in  
467 our conventional 1.5  $\mu$ s MD simulation trajectories. Our results agree with the functional data  
468 showing that KIIIA is a highly efficient but incomplete pore blocker of Nav channels. Study of the  
469 full binding and blocking mechanism of KIIIA on Nav channels is beyond the scope of this study  
470 and will require much longer simulation times or enhanced sampling techniques, and a structure  
471 of KIIIA bound to an open and conductive state of Nav channel, which is not currently available.  
472 Our MD simulations results reflect dynamics of the binding configuration captured in our KIIIA -

473 hNav1.7 model and the KIIIA - hNav1.2 structure to provide a more comprehensive insights into  
474 KIIIA – Nav channel interactions that extend beyond interpretation from the static structures.

475  
476 We used an integrative Rosetta computational modeling, functional characterization, and MD  
477 simulations approach to study molecular determinants of peptide toxin – Nav channel interactions.  
478 Establishing successful predictions with computational modeling is a critical step towards  
479 computational design of selective and potent peptide-based therapeutics. Our approach can be  
480 potentially expanded to rational design of novel peptides to target the extracellular pore vestibule  
481 region of Nav channels. Despite the high sequence conservation in the pore region of Nav channels,  
482 our work shows that specific sequence differences between Nav channels in the extracellular loop  
483 regions and the P2-helices of the pore can have important functional consequences on toxin –  
484 channel interaction. Rosetta protein design (Kuhlman et al., 2003; Cao et al., 2020; Leman et al.,  
485 2020) and optimization (Silva et al., 2019; Linsky et al., 2020) informed by these structural insights  
486 could potentially lead to development of high-affinity and specificity peptide inhibitors of Nav  
487 channels, forming a new class of biologics to treat Nav channel related diseases.

488

## 489 **Conclusions**

490 We generated a structural model of the conotoxin KIIIA in complex with hNav1.7 using homology  
491 modeling and docking simulations. Our model was validated with functional testing, using alanine-  
492 scan mutagenesis of KIIIA and hNav1.7, double mutant cycle analysis of specific pairwise toxin  
493 – channel interactions, supporting that acidic residues E919 and D923 on the P2-helix in DII of  
494 Nav1.7 significantly contribute to toxin – channel interaction, and that KIIIA forms multiple

495 interactions with the extracellular loops in DI-III. The published structure of the KIIIA - hNav1.2  
496 complex further supports predictions observed in our model. Unbiased MD simulations of KIIIA  
497 - hNav1.7 and KIIIA - hNav1.2 complexes suggest a potential important role of I1399 on the P2  
498 helix in DIII of hNav1.7 that may underlie the structural basis of KIIIA block of hNav1.7  
499 conductance. Overall, our results further characterize the molecular determinants of the KIIIA  
500 interaction with human Nav channels and can be potentially useful for rational design of increases  
501 in the potency or relative selectivity towards Nav1.7. As Nav1.7 is a drug target for pain (Payandeh  
502 and Hackos, 2018; Bennett et al., 2019; Dib-Hajj and Waxman, 2019), such optimization of KIIIA  
503 could result in novel peptide-based therapeutics.

504

## 505 **Acknowledgements**

506 We would like to thank Drs. Heike Wulff, Jie Zheng, and Igor Vorobyov, and members of Yarov-  
507 Yarovoy and Sack laboratories for helpful discussions. We thank Dr. Nieng Yan (Princeton  
508 University) for independent comparison of our KIIIA – hNav1.7 model to coordinates of KIIIA –  
509 hNav1.2 structure (Pan et al., 2019) prior to release in Protein Data Bank, and sharing the  
510 coordinates of electric eel and human Nav1.2 channel structures. We thank Dr. Christoph Lossin  
511 (University of California, Davis) for providing the hNav1.7 cell line and WT-hNav1.7 channel  
512 construct, as well as Dr. William Catterall (University of Washington) for the tsa201 cell line.  
513 Anton 2 computer time was provided by the Pittsburgh Supercomputing Center (PSC) through  
514 Grant R01GM116961 from the National Institutes of Health. The Anton 2 machine (Shaw et al.,  
515 2014) at PSC was generously made available by D.E. Shaw Research. This research was supported  
516 by U.S. National Institutes of Health awards U01HL126273 and R01HL128537 to VYY,

- 517 R01NS096317 to JTS, UC Davis Academic Senate Award FL18YAR to VYY, NIH T32
- 518 GM099608 to IHK, and AHA 17PRE33670204 to IHK.

## 519 **Materials and methods**

### 520 **Homology modeling of hNav1.7 based on EeNav1.4 structure**

521 The cryo-EM structure of the Nav1.4- $\beta$ 1 complex from the electric eel (eeNav1.4) (PDB ID:  
522 5XSY) (Yan et al., 2017) was used to generate the model of hNav1.7 channel using Rosetta  
523 structural modeling software (Song et al., 2013; Bender et al., 2016). **Initially, we refined the**  
524 **published coordinates of eeNav1.4, without the  $\beta$ 1 subunit by using the Rosetta cryo-EM**  
525 **refinement protocol (Wang et al., 2016) and picked the lowest scoring density-refitted eeNav1.4**  
526 **model to use as a template. The comparative modeling protocol RosettaCM (Song et al., 2013)**  
527 **was then used in combination with the electron density of the eeNav1.4 to model the hNav1.7**  
528 **structure. We generated 5,000 structural models of hNav1.7 and selected the top 500 lowest-**  
529 **scoring models for clustering analysis as described previously (Bonneau et al., 2002). Visual**  
530 **inspection of the top scoring clustered models was used to select the final model for the docking**  
531 **study.**

532

### 533 **Molecular docking of KIIIA to the hNav1.7 model**

534 The solution NMR structure of KIIIA (PDB ID: 2LXG) (Khoo et al., 2012) was used as an  
535 ensemble to dock to the hNav1.7 model using Rosetta protein-protein docking approach  
536 (Fleishman et al., 2011; Bender et al., 2016). By default, Rosetta moves proteins apart at the  
537 beginning of the protein-protein docking procedure which led to placement of KIIIA above the  
538 extracellular pore loops and did not allow sampling of the KIIIA binding site within the selectivity  
539 filter region because the KIIIA was not able to pass the narrow passage created by the extracellular  
540 pore loops. To address this problem, we subsequently divided the docking protocol into two stages

541 (see details of Rosetta commands and scripts in Supplementary File 1). In stage 1, docking was  
542 performed with the DI S5P1 and DIII S5P1 loops truncated, and full random translational and  
543 rotational perturbation of KIIIA at both low and high-resolution phases. This stage generated  
544 20,000 structural models of the docking complexes. We then selected the top 1,000 models based  
545 on the total scores and filtered based on the Rosetta  $\Delta\Delta G$  (an estimate of the binding energy of a  
546 complex) to select the top 500 models.  $\Delta\Delta G$  is computed by taking the difference of the energy of  
547 the KIIIA – hNav1.7 complex and of the separated KIIIA and hNav1.7 structures. We clustered  
548 these complexes using the Rosetta legacy clustering application. The center models of top 20  
549 clusters then passed to stage 2 docking. In this stage, positions of KIIIA in the top 20 clusters were  
550 used to create 20 different starting docking trajectories with the full structure of hNav1.7 model  
551 including all the extracellular loop regions. The full translational and rotational perturbation used  
552 in the previous stage was turned off. Instead, only limited local perturbation was allowed in both  
553 centroid and full-atom refinement phases. Similar to stage 1, we generated 20,000 structural  
554 docking models and filtered based on the Rosetta total score and  $\Delta\Delta G$  to select the top 500 models,  
555 which were again clustered to finalize the top 5 complexes for visual inspection. The selected  
556 docking model presented here (see coordinates of our KIIIA – hNav1.7 model in Supplement File  
557 – Model 1) is the only one in the top 5 clusters models that has KIIIA partially occluding the pore  
558 and K7 near the selectivity filter in agreement with experimental data demonstrating the  
559 contribution of K7 to binding affinity and percentage block (Zhang et al., 2007; McArthur et al.,  
560 2011).

561

562 **Molecular dynamics simulation of KIIIA - hNav1.7 and KIIIA - hNav1.2 complexes**



563 The docking complex of KIIIA - hNav1.7 and the cryo-EM structure of hNav1.2 (PDB ID: 6J8E)  
564 were used to setup systems for MD simulations. For the hNav1.2 structure, Rosetta density  
565 refinement protocol was applied as described above for the hNav1.7. The missing region on DI  
566 extracellular loop was modeled using Rosetta loop modeling. We placed one sodium ion in the  
567 selectivity filter and one in the cavity of the channels as initial setup for both simulations.  
568 CHARMM-GUI (Jo et al., 2008) was used to embed the KIIIA - hNav1.7 model and the KIIIA -  
569 hNav1.2 structure (PDB ID: 6J8E) in a lipid bilayer of POPC with explicit TIP3P water molecules  
570 at a concentration of 150 mM NaCl. CHARMM36 forcefield was used for proteins, lipids, ions,  
571 and waters in both systems. Each system contains approximately of 164,000 atoms. Protonation  
572 state is assigned at neutral pH. N-epsilon nitrogen of H12 on KIIIA is protonated instead of N-  
573 delta nitrogen as suggested in both the Rosetta model of hNav1.7 – KIIIA and the hNav1.2 – KIIIA  
574 structure. The C-terminal of KIIIA is amidated to be consistent with the KIIIA variant used in our  
575 experiments.

576  
577 Equilibrations were run on our local GPU cluster using NAMD version 2.12 (Jiang et al., 2011).  
578 After 10,000 steps of steepest descent minimization, MD simulations started with a timestep of 1  
579 fs with harmonic restraints initially applied to protein heavy atoms and some lipid tail dihedral  
580 angles as suggested by CHARMM-GUI (Jo et al., 2008). These restraints were slowly released  
581 over 2 ns. Harmonic restraints ( $0.1 \text{ kcal/mol/\AA}^2$ ) were then applied only to protein backbone atoms,  
582 and the systems were equilibrated further for 20 ns with a timestep of 2 fs. All bonds to H atoms  
583 were constrained using the SHAKE algorithm in order to use a 2 fs timestep. Simulations were  
584 performed in NPT ensemble with semi-isotropic pressure coupling to maintain the correct area per  
585 lipid, and constant temperature of 303.15 K. Particle Mesh Ewald (PME) method was used to

586 compute electrostatic interactions. Non-bonded pair lists were updated every 10 steps with a list  
587 cutoff distance of 16 Å and a real space cutoff of 12 Å with energy switching starting at 10 Å.

588 [Independent simulation systems were created by using different seed numbers in the equilibrations.](#)

589

590 We used the Anton 2 software version 1.31.0 for production runs of each system on the Anton 2  
591 supercomputer. [We ran 3 independent simulations of 1.5 μs for our hNav1.7 – KIIIA model and 3](#)  
592 [independent simulations of 1 μs for the hNav1.2 – KIIIA structure.](#) Simulations were performed  
593 in the NPT ensemble at 303.15 K A with 2 fs timestep. Non-bonded long-range interactions  
594 computed every 6 fs using the RESPA multiple time step algorithm. The multi-integrator algorithm  
595 was used for temperature and semi-isotropic pressure coupling and the u-series algorithm was used  
596 for long-range electrostatic interactions. A long-range Lennard-Jones (LJ) correction (beyond  
597 cutoff) was not used as was suggested for CHARMM36 lipid force field.

598

599 **Modeling of KIIIA - hNav1.7 complex using NavAb structure:** We previously performed  
600 [homology modeling of human Nav channels based on bacterial Nav channel structure before any](#)  
601 [eukaryotic Nav channel structures were published. We first generated a model of hNav1.4 pore](#)  
602 [using x-ray structure of the bacterial Nav channel NavAb \(PDB ID: 3RVY\) as a template using](#)  
603 [Rosetta homology modeling \(Bender et al., 2016\). We selected to first model Nav1.4 channel](#)  
604 [because of availability of experimental data on conotoxin – Nav channel interactions for model](#)  
605 [validation \(Dudley et al., 2000; Choudhary et al., 2007\). The extracellular loop regions in hNav1.4](#)  
606 [pore model were truncated and the P2 loops were rebuilt \*de novo\* using the Rosetta homology](#)  
607 [modeling \(Bender et al., 2016\). We used available experimental data for conotoxin GIIIA](#)

608 (homolog of KIIIA) interaction with Nav1.4 channel (Dudley et al., 2000; Choudhary et al., 2007)  
609 to guide the docking of GIIIA to hNav1.4 model. Specifically, charged residues R13 and K16 on  
610 GIIIA were biased to interact with acidic residues on the Nav1.4 P2 helices during docking using  
611 Rosetta bounded restraints (Bender et al., 2016). We then used the top GIIIA - hNav1.4 model that  
612 agreed with experimental data (Dudley et al., 2000; Choudhary et al., 2007) to build a model of  
613 GIIIA - hNav1.7 complex using Rosetta homology modeling (Bender et al., 2016). To create the  
614 initial configuration for KIIIA docking, we superimposed KIIIA onto GIIIA based on GIIIA -  
615 hNav1.7 complex model. In this final docking step, KIIIA was docked using only full-atom  
616 docking perturbations following by a flexible backbone refinement using Rosetta FlexPepDock  
617 (Raveh et al., 2010) and the best model was selected using Rosetta interface score. We did not  
618 perform experimental characterization on NavAb based KIIIA - hNav1.7 complex model because  
619 the subsequently published structures of eukaryotic Nav channels have allowed us to perform  
620 higher accuracy homology modeling of hNav1.7 based on eeNav1.4 structure (described above).

621

## 622 **Cell culture, transfection, and preparation**

623 Electrophysiology experiments were performed on transiently transfected tsa-201 cells (gift from  
624 William Catterall) and a HEK 293T cell line stably expressing hNav1.7 (gift from Chris Lossin).  
625 Cells were grown at 37°C, 5% CO<sub>2</sub> in DMEM with 4.5g/L D-glucose, L-glutamine, and 110 mg/L  
626 Sodium Pyruvate (Gibco cat# 11995-065) with 10% FBS, and 100 units/mL  
627 Penicillin/Streptomycin (Gibco cat# 15140-122). The stable cell line was raised in the same  
628 conditions with 500 µg/mL G418 as a selection agent. Cells were grown to 70% confluency in  
629 35mm dishes and passaged every 2-3 days for tsa-201 and 3-4 days for the stable-cell line. Cells  
630 were washed with divalent-free DPBS (Gibco cat# 14190-144) and dissociated with 0.05%

631 Trypsin-EDTA (Gibco cat# 25300-054) and seeded to fresh dishes with pre-warmed media. tsa-  
632 201 cells were transfected via Lipofectamine 2000 24-48 hours prior to experiments with 1  $\mu\text{g}$   
633 pCMV6-SCN9A (gift from Dr. Christoph Lossin) and 0.5  $\mu\text{g}$  pMaxGFP (Lonza) for identification  
634 of transfected cells. Mutant constructs were purchased, and coding sequences verified by  
635 Mutagenex. Prior to experiments, cells were washed with DPBS and dissociated in 1mL Versene  
636 (Gibco cat# 15040-066) and scraped from the dishes and transferred to a 14mL conical tube with  
637 3 mL DMEM. They were centrifuged at 1000 x g for 2 minutes and resuspended in a microfuge  
638 tube in 1mL extracellular solution (described below) with 10 mM D-glucose and rotated at RT  
639 until use.

640

#### 641 **Electrophysiology**

642 Whole-cell voltage-clamp recordings were performed at RT (21-22°C) in an RC-24N recording  
643 chamber fixed to a glass coverslip (Warner Instruments), mounted on a Zeiss Axiovert 35  
644 microscope illuminated with a Zeiss HBO 100W AttoArc lamp and filter set for epifluorescent  
645 detection of GFP expressing cells. Approximately 40  $\mu\text{L}$  of cell suspension was added to the pre-  
646 filled chamber and allowed to adhere to the glass bottomed chamber for 2-10 minutes. Fresh  
647 external solution was perfused through the chamber prior to patching. Borosilicate pipettes (1.5  
648 mm OD, 0.86 mm ID, Sutter instruments cat # BF150-86-7.5HP) were pulled, fire-polished, coated  
649 with Sylgard. [Tip resistances were 1-2 M \$\Omega\$ , when filled with the internal recording solution. GFP](#)  
650 [expressing cells were patched and signals were amplified with an Axon Axopatch 200-B](#)  
651 [\(Molecular Devices\) and acquired with an Instrutech LIH 8+8 ADC board \(HEKA\).](#) G $\Omega$  seals  
652 were obtained, and pipette capacitance was corrected for prior to break-in achieved by suction.  
653 Access resistance ( $R_s$ ) was typically 1-4 M $\Omega$ . 60%-80%  $R_s$  compensation (10  $\mu\text{s}$  lag) and

654 prediction was used to reduce voltage error to less than 10 mV as determined from the product of  
655 the peak current and  $R_s$  with compensation. P/5 leak subtraction protocol was used during  
656 recording. Signals were pre-filtered with a low-pass Bessel filter at 5 or 10 kHz before digitizing  
657 at 20 kHz and recorded with Patchmaster (HEKA, version 2x90.2) on a Windows 7 PC. The  
658 solutions were as follows in mM: External 3.5 KCl, 155 NaCl, 10 HEPES, 1 MgCl<sub>2</sub>, 1.5 CaCl<sub>2</sub>  
659 adjusted to pH 7.4 with NaOH, and 315 mOsm; Internal: 35 NaCl, 70 CsCl, 50 CsF, 1 EGTA, 10  
660 HEPES adjusted to pH 7.4 with CsOH at 310 mOsm. After break-in, cells were held at -120 mV  
661 and tested for stable Na<sup>+</sup> current with depolarizing 35 ms voltage steps to -10 mV from -120 mV  
662 collected every 5 s for up to 5 minutes to allow for a stable level of current prior to vehicle addition.  
663 Once stable current levels were achieved, 150  $\mu$ L of vehicle was manually added to the bath with  
664 displaced solution removed via an overflow vacuum line. After approximately 5 minutes, whole  
665 cell parameters were checked, and toxin (described below) was added by the same method as  
666 vehicle. Once apparent block plateaued, whole cell parameters were checked and adjusted as  
667 necessary, and pulsing resumed. To measure dissociation, gravity-fed perfusion with fresh external  
668 solution was started at a rate 1-2 mL/min during recording. Cells with stable leak and  $R_s$  allowing  
669 fitting to a single-exponential function (see below) throughout the experiment were included for  
670 analysis.

671

## 672 **Toxin preparation**

673 Lyophilized WT-KIIIA was purchased (Alomone labs, Jerusalem, IS), reconstituted in water and  
674 stored as 100  $\mu$ M stock aliquots at -80°C prior to use. Toxin variants were produced by solid state  
675 synthesis as described previously (Zhang et al., 2007) and stored as stock aliquots at -80°C prior  
676 to use. Stock concentrations were checked by 280nm absorbance on a Nanodrop 2000

677 spectrophotometer (ThermoFisher) with extinction coefficients determined by the ExPASy  
678 ProtParam online tool (Gasteiger et al., 2005). Stock aliquots of toxin were diluted in equal  
679 volumes of 2x External solution with 0.2% BSA for working solutions of toxin in vehicle of 1x  
680 External solution with 0.1% BSA and further diluted in 1x vehicle to the working concentration.  
681 Vehicle for controls were prepared in the same manner.

682

### 683 **Modeling and simulation analysis**

684 Structural modeling data were analyzed using Rosetta and rendered using UCSF Chimera  
685 (Pettersen et al., 2004), VMD (Humphrey et al., 1996) was used to analyze MD simulation data.  
686 All data were plotted in R using ggplot2 (Hadley, 2016).

687 *Tunnel detection for KIIIA block (Figure 1C):* We used CAVER (version 3.0) (Chovancova  
688 et al., 2012) to detect tunnels passing by KIIIA. Coordinates of Lys 7 in KIIIA were used as a  
689 searching starting point with probe\_radius 0.9, shell\_radius 5.0, shell\_depth 4.0 and max\_distance  
690 10. Multiple tunnels were detected for the whole structures. We visually select only tunnels that  
691 have maximum radii greater than 2 and neighboring KIIIA for presentation.

692 *Fractional contacts (Figure 5):* Fractional contact is defined as probability of finding two  
693 residues, one on the KIIIA and one on the channel forming contacts over time course of simulation.  
694 We considered two residues are in contact if any heavy atoms of one residue is within 4 Å of any  
695 heavy atoms of the other residues. Only contacts that have probability greater than 0.25 are shown  
696 for clarity.

697 *Interface RMSD (Figure 5 – figure supplement 1):* We used 10 Å as a cutoff for interface  
698 calculation between KIIIA and the channels. The interface is comprised of the KIIIA itself and

699 channel residues that are within 10 Å of KIIIA heavy atoms, defined at the beginning of the  
700 simulations. Backbone heavy atoms of the interface were used for RMSD calculation.

701

## 702 **Electrophysiology analysis**

703 Electrophysiology data were analyzed and plotted in IGOR 7 Pro (Wavemetrics). Geometric  
704 means of kinetic parameters were determined using Excel (Microsoft) and plotted in IGOR 7 Pro.  
705 Curve fitting was performed in IGOR Pro 7 as described previously (Dockendorff et al., 2018). To  
706 determine time constants of toxin association and dissociation ( $\tau_{on}$  and  $\tau_{off}$ , respectively), peak  
707 currents during depolarizing voltage steps were plotted by time, and data were fit with a single  
708 exponential function:

$$709 \quad [1] \quad I_{Na^+} = I_{Na^+_0} + Ae^{-t-t_0/\tau}$$

710 The association rate  $k_{on}$  was determined by equation 2, or equation 3 (McArthur et al., 2011) was  
711 used for KIIIA- variant H12A where the maximal block at saturating concentrations ( $F_{block}$ ) was  
712 already known and  $k_{off}$  could not be determined independently:

$$713 \quad [2] \quad k_{on} = \frac{1 - k_{off}}{\tau_{on} [tox]},$$

$$714 \quad [3] \quad k_{on} = \frac{F_{[tox]}}{\tau_{on} * [tox]}$$

715  $k_{off}$  was determined by equation 4:

$$716 \quad [4] \quad k_{off} = \frac{1}{\tau_{off}}$$

717 Affinity was determined kinetically as the dissociation constant  $K_d$  via equation 5:

718 [5] 
$$K_d = \frac{k_{off}}{k_{on}}$$

719 The slow dissociation of WT-KIIIA from WT-hNav1.7 made measurement of  $k_{off}$  difficult due to  
720 limited recovery during the experiment, thus values shown here are estimates assuming eventual  
721 full recovery of the maximal current before toxin association. The resulting values of affinity are  
722 consistent with previous reporting of kinetic determination of affinity for this channel (McArthur  
723 et al., 2011). Maximal block and  $IC_{50}$  for WT-KIIIA x WT-hNav1.7 was determined from  
724 concentration-response of peak residual current at equilibrium with equation 6. The Hill coefficient  
725  $h$  was assumed to be 1 in accordance with a single binding site:

726 [6] 
$$F_{[Tox]} = \frac{F_{block}}{\left\{1 + \left(\frac{IC_{50}}{[Tox]}\right)^h\right\}}$$

727 Maximum fractional block at saturating concentrations was determined from kinetic data and  
728 observed block ( $F_{[tox]}$ ) for other channel and toxin variants, except where noted, according to  
729 equation 7 (McArthur et al., 2011):

730 [7] 
$$F_{block} = F_{[tox]} \left(1 + \frac{K_d}{[tox]}\right)$$

731 The low affinity of H12A hindered precise measurement of dissociation kinetics; both the rapid  
732 rate of dissociation, paired with the low degree of block limited the number of data points for  
733 fitting single exponential to the dissociation data. The dissociation rate is extrapolated from  
734 Fractional block assuming maximal block at saturating concentration of 0.877 as reported  
735 previously (McArthur et al., 2011). The E919Q x D11A condition suffered from this same  
736 difficulty, thus kinetic values reported assumed similar levels of block to those observed during  
737 the E919Q x WT-KIIIA condition (0.92, Table 3). The lack of effect of KIIIA-D11A on channel  
738 block suggests that any additive effect of the E919Q x D11A double mutant condition would not



739 reduce the level of block seen from WT-KIIIA on Nav1.7-E919Q. Any errors in estimation of  
740 maximal block with toxin variants or channel mutants did not affect the calculation  $K_d = k_{off} / k_{on}$ ,  
741 and thus did not affect the coupling coefficients and energies calculated for double-mutant cycle  
742 analysis which are derived from  $K_d = k_{off} / k_{on}$ .

743 Coupling coefficients ( $\Omega$ ) and energies ( $E_{coupling}$ ) were calculated from the dissociation constants  
744 of the four conditions for each cycle according to equations 8 and 9, respectively (Hidalgo and  
745 MacKinnon, 1995) where “ $K_{dwm}$ ” would represent the dissociation constant for WT-hNav1.7 x  
746 Toxin-variant condition:

747 [8]  $\Omega = \frac{K_{dww} * K_{dmm}}{K_{dwm} * K_{dmw}}$ , [9]  $E_{coupling} = -RT \ln \Omega$

748 *Descriptive statistics:* Arithmetic means and standard error were calculated for  $F_{block}$ , while  
749 logarithmically scaled kinetic parameters were summarized with geometric means and standard  
750 deviations. Standard errors of kinetic parameters were obtained for the tables as the dividend of  
751 the standard deviation and the square-root of the sample size for each toxin-channel pair, as noted  
752 in parentheses in each table. Errors for coupling coefficients and coupling energies were calculated  
753 by linear propagation of error from fractional standard deviations of the reported  $K_d$  values for the  
754 toxin – channel mutant pairs used to calculate the coupling coefficients.

## 755 **Figure Legends**

756

### 757 **Figure 1. Structural model of KIIIA - hNav1.7 features eccentric binding of toxin to the outer**

758 **pore. (A)** Structure and sequence of KIIIA (PDB: 2LXG) (Khoo et al., 2012) shows alpha helical

759 core stabilized by three disulfide bridges. **(B)** Extracellular view of our homology model of KIIIA

760 – hNav1.7 complex based on the EeNav1.4- $\beta$ 1 cryo-EM structure (Yan et al., 2017). Channel

761 domains are depicted according to color keys, and KIIIA is shown in magenta ribbon and surface.

762 KIIIA binds eccentrically to the outer pore between DII and DIII. **(C)** Incomplete block of KIIIA

763 revealed by side view of channel pore with KIIIA bound (magenta) and cavity volume. **(D)** Rosetta

764 alanine scan identified residues K7, W8, R10, H12, and R14 as significant contributors to binding

765 energy. **(E)** Heatmap of Rosetta  $\Delta\Delta G$  on KIIIA structure shows the importance of the helical region

766 for binding. **(F)** Close up views of key interactions at KIIIA – hNav1.7 interface.

### 767 **Figure 2. Functional studies of toxin variants and channel mutations.** **(A)** Normalized peak $I_{Na}$

768 from a whole cell voltage clamp experiment with 10  $\mu$ M WT-KIIIA against WT-hNav1.7 resulting

769 in incomplete block and (inset) raw current traces before toxin (black) and after toxin (blue). **(B)**

770 Hill-fit (black) and 95% confidence interval (dashed blue) of concentration-response data for WT-

771 KIIIA against hNav1.7 in HEK293 cells ( $IC_{50}=0.41\pm 0.16$   $\mu$ M mean $\pm$ SD, n=2-4 cells per

772 concentration), from maximum block recorded during association experiments. Empty circles

773 represent single cells. **(C)** Calculated Fractional block (see Materials and methods) for toxin

774 variants and channel mutants (mean $\pm$ SEM). † WT x H12A block data were reported previously

775 (McArthur et al., 2011). **(D)** Kinetic data from electrophysiological measurements show general

776 agreement with Rosetta predicted energies. Alanine variants of residues K7, W8, D11, and H12

777 showed significant reductions in affinity ( $K_d$ )(left), little change in association ( $k_{on}$ )(middle), but

778 marked increases in toxin dissociation ( $k_{off}$ )(right). Bars are geometric mean $\pm$ SD from n=3-5 cells  
779 per variant (reported in Table 1), empty circles represent single cells. (E) Mutations to channel  
780 residues demonstrate reductions in affinity of the WT-KIIIA from Y362C, E919Q, and D923A  
781 (left), little change to toxin association (middle), and increases in dissociation (right), similar to  
782 the effects of toxin variants. Bars are geometric mean $\pm$ SD from n=3-5 cells per variant (reported  
783 in table 2), empty circles represent single cells.

784 **Figure 3. Double mutant cycle analysis supports key pairwise interactions between KIIIA**  
785 **and hNav1.7. (A)** Thermodynamic double-mutant cycles between H12A x D923A, K7A x E919Q,  
786 and D11A x E919Q.  $K_d$  (geometric mean $\pm$ SEM) listed under each channel mutant/toxin variant  
787 pair tested. Center values are coupling energies (kcal $\cdot$ mol<sup>-1</sup>) for the interactions with errors from a  
788 linear propagation of error. (B)  $K_d$ ,  $k_{on}$ , and  $k_{off}$  for single and double mutants. Bars are geometric  
789 mean $\pm$ SD, n=2-5 cells per condition (reported in table 3), empty circles are individual cells. The  
790 double mutants for K7A x E919Q and H12A x D923A were similar to the respective single mutant  
791 conditions, while the D11A x E919Q double mutant showed a much greater reduction in affinity  
792 relative to the single mutants.

793 **Figure 4. Marked difference for KIIIA binding specificity among Nav channel isoforms. (A)**  
794 Comparisons of key residue interactions on the KIIIA - hNav1.7 model and the KIIIA - hNav1.2  
795 structure. Domains and residue labels are depicted according to color keys. (B) Sequence  
796 alignment of the different Nav subtypes at the interaction site with KIIIA. Different regions are  
797 labeled. Key interacting residues of KIIIA are labeled and colored in magenta at positions of  
798 corresponding interactions in channel residues. Superscripts show sequence number of hNav1.7.

799 **Figure 5. MD simulations of KIIIA - hNav1.7 and KIIIA - hNav1.2 complexes show**  
800 **structural dynamics of KIIIA interaction with hNav1.7 (A and C) and hNav1.2 (B and D).**

801 (A, B) Couplings of K7 with key acidic residues on the hNav P2 helices. Density projections of  
802 K7 (Nitrogen atom) and the acidic residue (oxygen atoms) on P2-helix (labeled) on the XY plane  
803 (upper panel). For clarity, densities of the acidic residues are shown as contour plots using kernel  
804 density estimation. Representative snapshots showing interactions of K7 with the acidic residues  
805 at high density regions (labeled) identified from the density projections (lower panel). (C, D)  
806 Heatmaps showing fractional contacts between key residues on KIIIA and hNav channels during  
807 the simulations.

808 **Figure 1—figure supplement 1. Rosetta models of hNav1.7 – KIIIA complex. Domains are**  
809 **depicted according to color keys.** (A) Extracellular view of the pore region of the Rosetta model  
810 of the KIIIA - hNav1.7 complex based on bacterial NavAb structure (Payandeh et al., 2011). (B)  
811 Extracellular view of the pore region of the KIIIA - hNav1.7 model based on eeNav1.4 structure  
812 (Yan et al., 2017) in superposition with the cryo-EM structure of the KIIIA - hNav1.2 complex  
813 (Pan et al., 2019).

814 **Figure 2—figure supplement 1. Representative data from functional studies of toxin variants**  
815 **and channel mutations.** (A) Normalized peak  $I_{Na^+}$  from a whole cell voltage clamp experiments  
816 with WT-hNav1.7 in the presence of toxin variants as stated in each plot, exponential fits of  
817 association and dissociation shown in blue. Raw current traces (inset) before toxin (black) and  
818 after toxin addition (blue). (B) Normalized peak  $I_{Na^+}$  from whole cell voltage clamp experiments  
819 with hNav1.7 mutants as labeled in the presence of WT-KIIIA as in panel A.

820 **Figure 3—figure supplement 1. Representative data from double-mutant cycle analysis.** (A)  
821 Normalized peak  $I_{Na^+}$  from a whole cell voltage clamp experiments with WT x WT, single, and  
822 double mutations D923A and H12A as indicated by column and row labels. Exponential fits of  
823 association and dissociation shown in blue. Raw current traces (inset) before toxin (black) and

824 after toxin addition (blue). **(B)** Normalized peak  $I_{Na^+}$  from a whole cell voltage clamp experiments,  
825 as in panel A for the two residue pairs E919 x K7 and E919 x D11.

826 **Figure 4—figure supplement 1. Differences in interactions of KIIIA residues D11 (left panel)**  
827 **and R10 (right panel) between the KIIIA - hNav1.7 model and the KIIIA - hNav1.2 structure.**

828 Domains and labels are depicted according to color keys. Both alternative sidechain rotamers of  
829 KIIIA R10 residue identified in the KIIIA - hNav1.2 structure are shown.

830 **Figure 5—figure supplement 1. MD simulation of KIIIA - hNav1.7 model and KIIIA –**  
831 **hNav1.2 structure. (A)** Interfacial RMSD of the KIIIA – hNav1.7 and KIIIA – hNav1.2  
832 complexes in different independent simulations. **(B)** Couplings of R10 with key acidic residues on  
833 the P2 helices of hNav1.7 (upper panel) and hNav1.2 (lower panel) depicted as density projections  
834 of R10 and the acidic residue on P2-helix (labeled) on the XY plane. For clarity, densities of the  
835 acidic residues are shown as contour plots using kernel density estimation.

836 **Figure 5—figure supplement 2. MD simulation of KIIIA - hNav1.7 model. (A)** Time series of  
837 representative contacts of K7 and R10 with acidic residues on P2 helix of hNav1.7. Labels show  
838 residue numbers and their associated atom names (in parenthesis). **(B)** A snapshot of the last frame  
839 of the 1 $\mu$ s simulation. Domains are depicted according to color keys and channel residues that  
840 have high fractional contacts in Figure 5A are shown in stick representation and labeled.

841 **Figure 5—figure supplement 3. MD simulation of KIIIA - hNav1.2 model. (A)** Time series of  
842 representative contacts of K7 and R10 with acidic residues on P2 helix of hNav1.7. Labels show  
843 residue numbers and their associated atom names (in parenthesis). **(B)** A snapshot of the last frame  
844 of the 1 $\mu$ s simulation. Domains are depicted according to color keys and channel residues that  
845 have high fractional contacts in Figure 5B are shown in stick representation and labeled.

## 846 **References**

- 847 Ahern, C.A., J. Payandeh, F. Bosmans, and B. Chanda. 2016. The hitchhiker's guide to the  
848 voltage-gated sodium channel galaxy. *J Gen Physiol.* 147:1-24.
- 849 Bender, B.J., A. Cisneros, 3rd, A.M. Duran, J.A. Finn, D. Fu, A.D. Lokits, B.K. Mueller, A.K.  
850 Sangha, M.F. Sauer, A.M. Sevy, G. Sliwoski, J.H. Sheehan, F. DiMaio, J. Meiler, and R.  
851 Moretti. 2016. Protocols for Molecular Modeling with Rosetta3 and RosettaScripts.  
852 *Biochemistry.* 55:4748-4763.
- 853 Bennett, D.L., A.J. Clark, J. Huang, S.G. Waxman, and S.D. Dib-Hajj. 2019. The Role of  
854 Voltage-Gated Sodium Channels in Pain Signaling. *Physiol Rev.* 99:1079-1151.
- 855 Bonneau, R., C.E. Strauss, C.A. Rohl, D. Chivian, P. Bradley, L. Malmstrom, T. Robertson, and  
856 D. Baker. 2002. De novo prediction of three-dimensional structures for major protein  
857 families. *J Mol Biol.* 322:65-78.
- 858 Cao, L., I. Goreshnik, B. Coventry, J.B. Case, L. Miller, L. Kozodoy, R.E. Chen, L. Carter, A.C.  
859 Walls, Y.J. Park, E.M. Strauch, L. Stewart, M.S. Diamond, D. Veessler, and D. Baker.  
860 2020. De novo design of picomolar SARS-CoV-2 miniprotein inhibitors. *Science.*  
861 370:426-431.
- 862 Catterall, W.A. 2014. Structure and function of voltage-gated sodium channels at atomic  
863 resolution. *Exp Physiol.* 99:35-51.
- 864 Catterall, W.A., A.L. Goldin, and S.G. Waxman. 2005. International Union of Pharmacology.  
865 XLVII. Nomenclature and structure-function relationships of voltage-gated sodium  
866 channels. *Pharmacol Rev.* 57:397-409.

- 867 Choudhary, G., M.P. Aliste, D.P. Tieleman, R.J. French, and S.C. Dudley, Jr. 2007. Docking of  
868 mu-conotoxin GIIIA in the sodium channel outer vestibule. *Channels (Austin)*. 1:344-  
869 352.
- 870 Chovancova, E., A. Pavelka, P. Benes, O. Strnad, J. Brezovsky, B. Kozlikova, A. Gora, V. Sustr,  
871 M. Klvana, P. Medek, L. Biedermannova, J. Sochor, and J. Damborsky. 2012. CAVER  
872 3.0: a tool for the analysis of transport pathways in dynamic protein structures. *PLoS*  
873 *Comput Biol.* 8:e1002708.
- 874 Dib-Hajj, S.D., and S.G. Waxman. 2019. Sodium Channels in Human Pain Disorders: Genetics  
875 and Pharmacogenomics. *Annu Rev Neurosci.*
- 876 Dib-Hajj, S.D., Y. Yang, J.A. Black, and S.G. Waxman. 2013. The Na(V)1.7 sodium channel:  
877 from molecule to man. *Nat Rev Neurosci.* 14:49-62.
- 878 Dockendorff, C., D.M. Gandhi, I.H. Kimball, K.S. Eum, R. Rusinova, H.I. Ingolfsson, R.  
879 Kapoor, T. Peyear, M.W. Dodge, S.F. Martin, R.W. Aldrich, O.S. Andersen, and J.T.  
880 Sack. 2018. Synthetic Analogues of the Snail Toxin 6-Bromo-2-mercaptotryptamine  
881 Dimer (BrMT) Reveal That Lipid Bilayer Perturbation Does Not Underlie Its Modulation  
882 of Voltage-Gated Potassium Channels. *Biochemistry.* 57:2733-2743.
- 883 Dudley, S.C., Jr., N. Chang, J. Hall, G. Lipkind, H.A. Fozzard, and R.J. French. 2000. mu-  
884 conotoxin GIIIA interactions with the voltage-gated Na(+) channel predict a clockwise  
885 arrangement of the domains. *J Gen Physiol.* 116:679-690.
- 886 Fleishman, S.J., A. Leaver-Fay, J.E. Corn, E.M. Strauch, S.D. Khare, N. Koga, J. Ashworth, P.  
887 Murphy, F. Richter, G. Lemmon, J. Meiler, and D. Baker. 2011. RosettaScripts: a  
888 scripting language interface to the Rosetta macromolecular modeling suite. *PloS one.*  
889 6:e20161.

- 890 French, R.J., D. Yoshikami, M.F. Sheets, and B.M. Olivera. 2010. The tetrodotoxin receptor of  
891 voltage-gated sodium channels--perspectives from interactions with micro-conotoxins.  
892 *Mar Drugs*. 8:2153-2161.
- 893 Gasteiger, E., C. Hoogland, A. Gattiker, S. Duvaud, M.R. Wilkins, R.D. Appel, and A. Bairoch.  
894 2005. Protein Identification and Analysis Tools on the ExPASy Server;. *In The*  
895 *Proteomics Protocols Handbook*. J.M. Walker, editor. Humana Press. 571-607.
- 896 Gilchrist, J., B.M. Olivera, and F. Bosmans. 2014. Animal toxins influence voltage-gated sodium  
897 channel function. *Handb Exp Pharmacol*. 221:203-229.
- 898 Gray, J.J., S. Moughon, C. Wang, O. Schueler-Furman, B. Kuhlman, C.A. Rohl, and D. Baker.  
899 2003. Protein-protein docking with simultaneous optimization of rigid-body displacement  
900 and side-chain conformations. *J Mol Biol*. 331:281-299.
- 901 Hadley, W. 2016. Ggplot2. Springer Science+Business Media, LLC, New York, NY. pages cm  
902 pp.
- 903 Hidalgo, P., and R. MacKinnon. 1995. Revealing the architecture of a K<sup>+</sup> channel pore through  
904 mutant cycles with a peptide inhibitor. *Science*. 268:307-310.
- 905 Hille, B. 2001. Ion Channels of Excitable Membranes. 3rd.ed. Sinauer Associates, Sunderland,  
906 MA).
- 907 Humphrey, W., A. Dalke, and K. Schulten. 1996. VMD: visual molecular dynamics. *J Mol*  
908 *Graph*. 14:33-38, 27-38.
- 909 Jiang, D., H. Shi, L. Tonggu, T.M. Gamal El-Din, M.J. Linaeus, Y. Zhao, C. Yoshioka, N.  
910 Zheng, and W.A. Catterall. 2020. Structure of the Cardiac Sodium Channel. *Cell*.  
911 180:122-134 e110.



- 912 Jiang, W., D.J. Hardy, J.C. Phillips, A.D. Mackerell, Jr., K. Schulten, and B. Roux. 2011. High-  
913 performance scalable molecular dynamics simulations of a polarizable force field based  
914 on classical Drude oscillators in NAMD. *J Phys Chem Lett.* 2:87-92.
- 915 Jo, S., T. Kim, V.G. Iyer, and W. Im. 2008. CHARMM-GUI: a web-based graphical user  
916 interface for CHARMM. *J Comput Chem.* 29:1859-1865.
- 917 Khoo, K.K., K. Gupta, B.R. Green, M.M. Zhang, M. Watkins, B.M. Olivera, P. Balaram, D.  
918 Yoshikami, G. Bulaj, and R.S. Norton. 2012. Distinct disulfide isomers of mu-conotoxins  
919 KIIIA and KIIIB block voltage-gated sodium channels. *Biochemistry.* 51:9826-9835.
- 920 Korkosh, V.S., B.S. Zhorov, and D.B. Tikhonov. 2014. Folding similarity of the outer pore  
921 region in prokaryotic and eukaryotic sodium channels revealed by docking of conotoxins  
922 GIIIA, PIIIA, and KIIIA in a NavAb-based model of Nav1.4. *J Gen Physiol.* 144:231-  
923 244.
- 924 Ku, H.H. 1966. Notes on the use of propagation of error formulas. *Journal of Research of the*  
925 *National Bureau of Standards. Section C: Engineering and Instrumentation.* 70C:263-  
926 272.
- 927 Kubota, T., T. Durek, B. Dang, R.K. Finol-Urdaneta, D.J. Craik, S.B. Kent, R.J. French, F.  
928 Bezanilla, and A.M. Correa. 2017. Mapping of voltage sensor positions in resting and  
929 inactivated mammalian sodium channels by LRET. *Proc Natl Acad Sci U S A.*  
930 114:E1857-E1865.
- 931 Kuhlman, B., G. Dantas, G.C. Ireton, G. Varani, B.L. Stoddard, and D. Baker. 2003. Design of a  
932 novel globular protein fold with atomic-level accuracy. *Science.* 302:1364-1368.
- 933 Leman, J.K., B.D. Weitzner, S.M. Lewis, J. Adolf-Bryfogle, N. Alam, R.F. Alford, M.  
934 Aprahamian, D. Baker, K.A. Barlow, P. Barth, B. Basanta, B.J. Bender, K. Blacklock, J.

935 Bonet, S.E. Boyken, P. Bradley, C. Bystroff, P. Conway, S. Cooper, B.E. Correia, B.  
936 Coventry, R. Das, R.M. De Jong, F. DiMaio, L. Dsilva, R. Dunbrack, A.S. Ford, B.  
937 Frenz, D.Y. Fu, C. Geniesse, L. Goldschmidt, R. Gowthaman, J.J. Gray, D. Gront, S.  
938 Guffy, S. Horowitz, P.S. Huang, T. Huber, T.M. Jacobs, J.R. Jeliazkov, D.K. Johnson, K.  
939 Kappel, J. Karanicolas, H. Khakzad, K.R. Khar, S.D. Khare, F. Khatib, A. Khramushin,  
940 I.C. King, R. Kleffner, B. Koepnick, T. Kortemme, G. Kuenze, B. Kuhlman, D. Kuroda,  
941 J.W. Labonte, J.K. Lai, G. Lapidoth, A. Leaver-Fay, S. Lindert, T. Linsky, N. London,  
942 J.H. Lubin, S. Lyskov, J. Maguire, L. Malmstrom, E. Marcos, O. Marcu, N.A. Marze, J.  
943 Meiler, R. Moretti, V.K. Mulligan, S. Nerli, C. Norn, S. O'Conchuir, N. Ollikainen, S.  
944 Ovchinnikov, M.S. Pacella, X. Pan, H. Park, R.E. Pavlovicz, M. Pethe, B.G. Pierce, K.B.  
945 Pilla, B. Raveh, P.D. Renfrew, S.S.R. Burman, A. Rubenstein, M.F. Sauer, A. Scheck,  
946 W. Schief, O. Schueler-Furman, Y. Sedan, A.M. Sevy, N.G. Sgourakis, L. Shi, J.B.  
947 Siegel, D.A. Silva, S. Smith, Y. Song, A. Stein, M. Szegedy, F.D. Teets, S.B. Thyme,  
948 R.Y. Wang, A. Watkins, L. Zimmerman, and R. Bonneau. 2020. Macromolecular  
949 modeling and design in Rosetta: recent methods and frameworks. *Nat Methods*. 17:665-  
950 680.

951 Linsky, T.W., R. Vergara, N. Codina, J.W. Nelson, M.J. Walker, W. Su, C.O. Barnes, T.Y.  
952 Hsiang, K. Esser-Nobis, K. Yu, Z.B. Reneer, Y.J. Hou, T. Priya, M. Mitsumoto, A. Pong,  
953 U.Y. Lau, M.L. Mason, J. Chen, A. Chen, T. Berrocal, H. Peng, N.S. Clairmont, J.  
954 Castellanos, Y.R. Lin, A. Josephson-Day, R.S. Baric, D.H. Fuller, C.D. Walkey, T.M.  
955 Ross, R. Swanson, P.J. Bjorkman, M. Gale, Jr., L.M. Blancas-Mejia, H.L. Yen, and D.A.  
956 Silva. 2020. De novo design of potent and resilient hACE2 decoys to neutralize SARS-  
957 CoV-2. *Science*. 370:1208-1214.

- 958 McArthur, J.R., G. Singh, D. McMaster, R. Winkfein, D.P. Tieleman, and R.J. French. 2011.  
959 Interactions of key charged residues contributing to selective block of neuronal sodium  
960 channels by mu-conotoxin KIIIA. *Mol Pharmacol.* 80:573-584.
- 961 Mulcahy, J.V., H. Pajouhesh, J.T. Beckley, A. Delwig, J. Du Bois, and J.C. Hunter. 2019.  
962 Challenges and Opportunities for Therapeutics Targeting the Voltage-Gated Sodium  
963 Channel Isoform Nav1.7. *J Med Chem.* 62:8695-8710.
- 964 Nguyen, P.T., K.R. DeMarco, I. Vorobyov, C.E. Clancy, and V. Yarov-Yarovoy. 2019.  
965 Structural basis for antiarrhythmic drug interactions with the human cardiac sodium  
966 channel. *Proc Natl Acad Sci U S A.* 116:2945-2954.
- 967 Pajouhesh, H., J.T. Beckley, A. Delwig, H.S. Hajare, G. Luu, D. Monteleone, X. Zhou, J. Ligutti,  
968 S. Amagasu, B.D. Moyer, D.C. Yeomans, J. Du Bois, and J.V. Mulcahy. 2020. Discovery  
969 of a selective, state-independent inhibitor of Nav1.7 by modification of guanidinium  
970 toxins. *Sci Rep.* 10:14791.
- 971 Pan, X., Z. Li, X. Huang, G. Huang, S. Gao, H. Shen, L. Liu, J. Lei, and N. Yan. 2019.  
972 Molecular basis for pore blockade of human Na(+) channel Nav1.2 by the mu-conotoxin  
973 KIIIA. *Science.* 363:1309-1313.
- 974 Pan, X., Z. Li, Q. Zhou, H. Shen, K. Wu, X. Huang, J. Chen, J. Zhang, X. Zhu, J. Lei, W. Xiong,  
975 H. Gong, B. Xiao, and N. Yan. 2018. Structure of the human voltage-gated sodium  
976 channel Nav1.4 in complex with beta1. *Science.*
- 977 Payandeh, J., and D.H. Hackos. 2018. Selective Ligands and Drug Discovery Targeting the  
978 Voltage-Gated Sodium Channel Nav1.7. *Handb Exp Pharmacol.* 246:271-306.
- 979 Payandeh, J., T. Scheuer, N. Zheng, and W.A. Catterall. 2011. The crystal structure of a voltage-  
980 gated sodium channel. *Nature.* 475:353-358.

981 Pettersen, E.F., T.D. Goddard, C.C. Huang, G.S. Couch, D.M. Greenblatt, E.C. Meng, and T.E.  
982 Ferrin. 2004. UCSF Chimera--a visualization system for exploratory research and  
983 analysis. *J Comput Chem.* 25:1605-1612.

984 Ragsdale, D.S., J.C. McPhee, T. Scheuer, and W.A. Catterall. 1994. Molecular determinants of  
985 state-dependent block of Na<sup>+</sup> channels by local anesthetics. *Science.* 265:1724-1728.

986 Ranganathan, R., J.H. Lewis, and R. MacKinnon. 1996. Spatial localization of the K<sup>+</sup> channel  
987 selectivity filter by mutant cycle-based structure analysis. *Neuron.* 16:131-139.

988 Raveh, B., N. London, and O. Schueler-Furman. 2010. Sub-angstrom modeling of complexes  
989 between flexible peptides and globular proteins. *Proteins.* 78:2029-2040.

990 Schreiber, G., and A.R. Fersht. 1995. Energetics of protein-protein interactions: Analysis of the  
991 Barnase-Barstar interface by single mutations and double mutant cycles. *Journal of*  
992 *Molecular Biology.* 248:478-486.

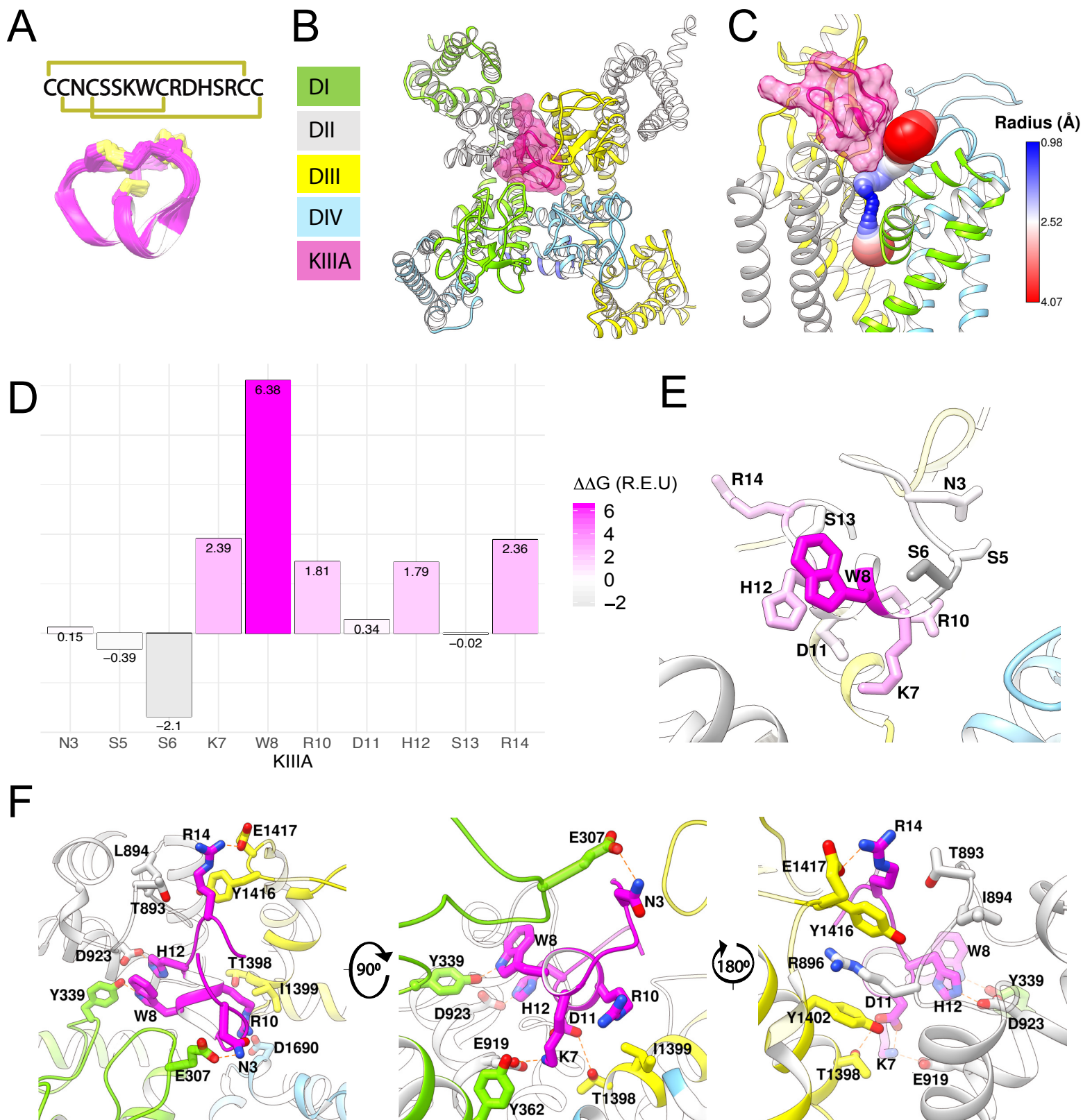
993 Shaw, D.E., J.P. Grossman, J.A. Bank, B. Batson, J.A. Butts, J.C. Chao, M.M. Deneroff, R.O.  
994 Dror, A. Even, C.H. Fenton, A. Forte, J. Gagliardo, G. Gill, B. Greskamp, C.R. Ho, D.J.  
995 Ierardi, L. Iserovich, J.S. Kuskin, R.H. Larson, T. Layman, L.S. Lee, A.K. Lerer, C. Li,  
996 D. Killebrew, K.M. Mackenzie, S.Y.H. Mok, M.A. Moraes, R. Mueller, L.J. Nociolo,  
997 J.L. Peticolas, T. Quan, D. Ramot, J.K. Salmon, D.P. Scarpazza, U. Ben Schafer, N.  
998 Siddique, C.W. Snyder, J. Spengler, P.T.P. Tang, M. Theobald, H. Toma, B. Towles, B.  
999 Vitale, S.C. Wang, and C. Young. 2014. Anton 2: Raising the bar for performance and  
1000 programmability in a special-purpose molecular dynamics supercomputer. *Sci14:*  
1001 *International Conference for High Performance Computing, Networking, Storage and*  
1002 *Analysis.*41-53.

- 1003 Shen, H., Z. Li, Y. Jiang, X. Pan, J. Wu, B. Cristofori-Armstrong, J.J. Smith, Y.K.Y. Chin, J.  
1004 Lei, Q. Zhou, G.F. King, and N. Yan. 2018. Structural basis for the modulation of  
1005 voltage-gated sodium channels by animal toxins. *Science*.
- 1006 Shen, H., D. Liu, K. Wu, J. Lei, and N. Yan. 2019. Structures of human Nav1.7 channel in  
1007 complex with auxiliary subunits and animal toxins. *Science*. 363:1303-1308.
- 1008 Silva, D.A., S. Yu, U.Y. Ulge, J.B. Spangler, K.M. Jude, C. Labao-Almeida, L.R. Ali, A.  
1009 Quijano-Rubio, M. Ruterbusch, I. Leung, T. Biary, S.J. Crowley, E. Marcos, C.D.  
1010 Walkey, B.D. Weitzner, F. Pardo-Avila, J. Castellanos, L. Carter, L. Stewart, S.R.  
1011 Riddell, M. Pepper, G.J.L. Bernardes, M. Dougan, K.C. Garcia, and D. Baker. 2019. De  
1012 novo design of potent and selective mimics of IL-2 and IL-15. *Nature*. 565:186-191.
- 1013 SiteOne Therapeutics, I. 2021. A Phase 1, Randomized, Double-Blind, Placebo-Controlled  
1014 Single Ascending Dose Study to Evaluate the Safety, Tolerability, and Pharmacokinetics  
1015 of ST-2427 IV Infusion in Healthy Subjects. *In* National Library of Medicine. USA.
- 1016 Song, Y., F. DiMaio, R.Y. Wang, D. Kim, C. Miles, T. Brunette, J. Thompson, and D. Baker.  
1017 2013. High-resolution comparative modeling with RosettaCM. *Structure*. 21:1735-1742.
- 1018 Wang, C., P. Bradley, and D. Baker. 2007. Protein-protein docking with backbone flexibility. *J*  
1019 *Mol Biol*. 373:503-519.
- 1020 Wang, R.Y., Y. Song, B.A. Barad, Y. Cheng, J.S. Fraser, and F. DiMaio. 2016. Automated  
1021 structure refinement of macromolecular assemblies from cryo-EM maps using Rosetta.  
1022 *Elife*. 5.
- 1023 Wilson, M.J., D. Yoshikami, L. Azam, J. Gajewiak, B.M. Olivera, G. Bulaj, and M.M. Zhang.  
1024 2011.  $\mu$ -Conotoxins that differentially block sodium channels NaV1.1 through 1.8

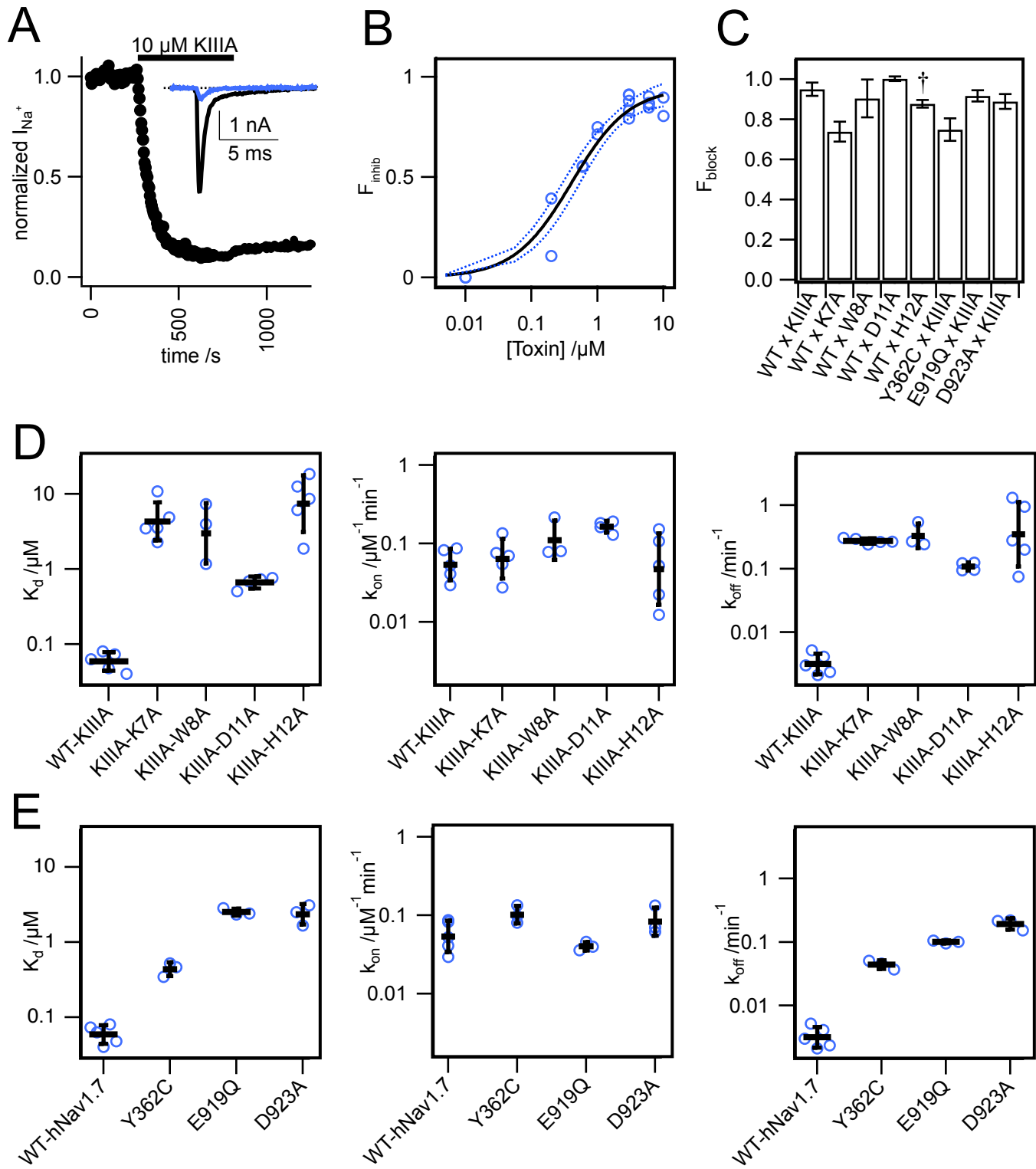
- 1025 identify those responsible for action potentials in sciatic nerve. *Proc Natl Acad Sci U S A*.
- 1026 108:10302-10307.
- 1027 Yan, Z., Q. Zhou, L. Wang, J. Wu, Y. Zhao, G. Huang, W. Peng, H. Shen, J. Lei, and N. Yan.
- 1028 2017. Structure of the Nav1.4-beta1 Complex from Electric Eel. *Cell*. 170:470-482 e411.
- 1029 Yarov-Yarovoy, V., J. Brown, E.M. Sharp, J.J. Clare, T. Scheuer, and W.A. Catterall. 2001.
- 1030 Molecular determinants of voltage-dependent gating and binding of pore-blocking drugs
- 1031 in transmembrane segment IIS6 of the Na(+) channel alpha subunit. *J Biol Chem*.
- 1032 276:20-27.
- 1033 Yarov-Yarovoy, V., J.C. McPhee, D. Idsvoog, C. Pate, T. Scheuer, and W.A. Catterall. 2002.
- 1034 Role of amino acid residues in transmembrane segments IS6 and IIS6 of the Na+ channel
- 1035 alpha subunit in voltage-dependent gating and drug block. *J Biol Chem*. 277:35393-
- 1036 35401.
- 1037 Zhang, M.M., B.R. Green, P. Catlin, B. Fiedler, L. Azam, A. Chadwick, H. Terlau, J.R.
- 1038 McArthur, R.J. French, J. Gulyas, J.E. Rivier, B.J. Smith, R.S. Norton, B.M. Olivera, D.
- 1039 Yoshikami, and G. Bulaj. 2007. Structure/function characterization of micro-conotoxin
- 1040 KIIIA, an analgesic, nearly irreversible blocker of mammalian neuronal sodium channels.
- 1041 *J Biol Chem*. 282:30699-30706.
- 1042 Zhang, M.M., J.R. McArthur, L. Azam, G. Bulaj, B.M. Olivera, R.J. French, and D. Yoshikami.
- 1043 2009. Synergistic and antagonistic interactions between tetrodotoxin and mu-conotoxin in
- 1044 blocking voltage-gated sodium channels. *Channels (Austin)*. 3:32-38.
- 1045



Figure 1



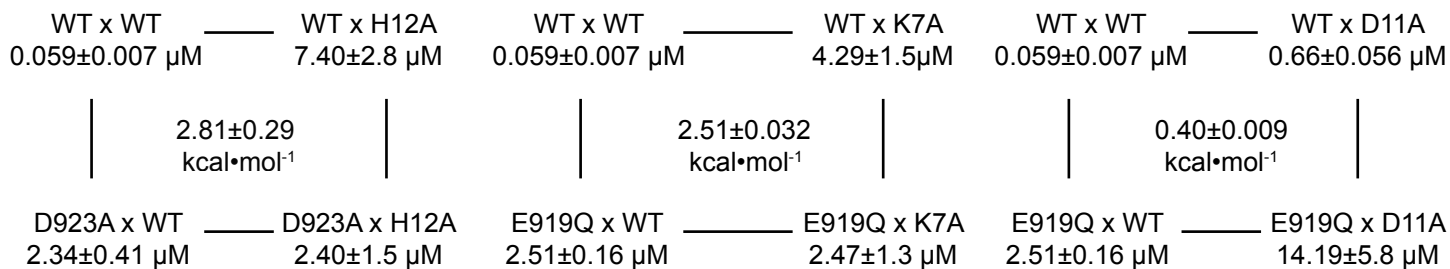
## Figure 2



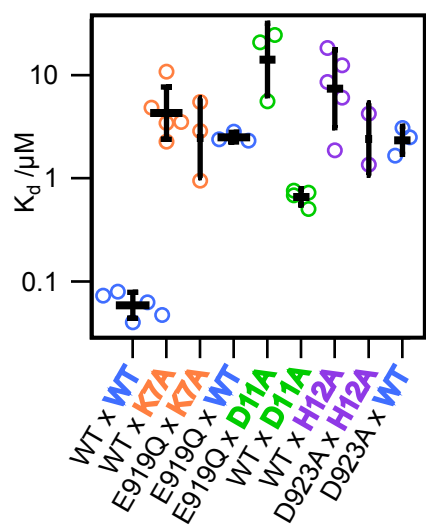


### Figure 3

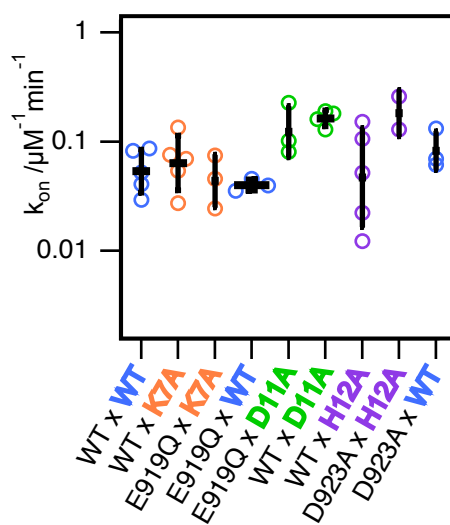
**A**



**B**



**C**



**D**

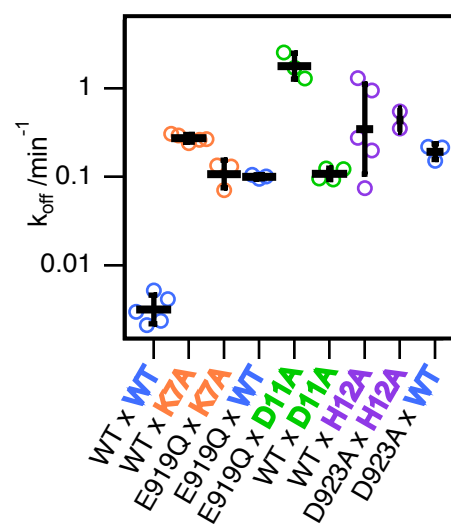
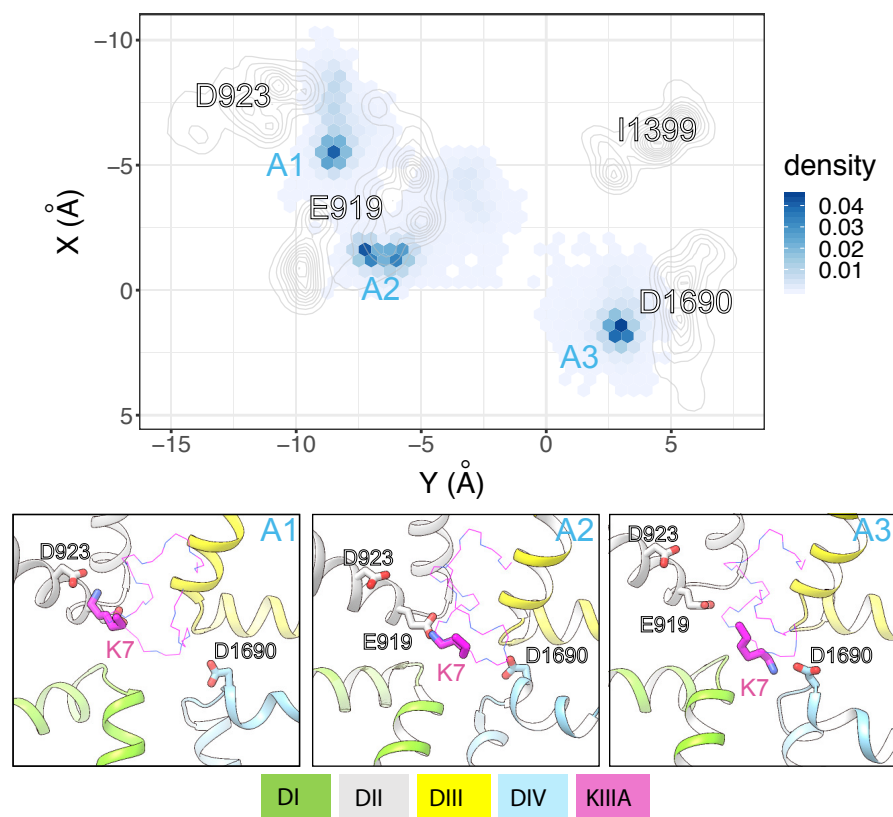


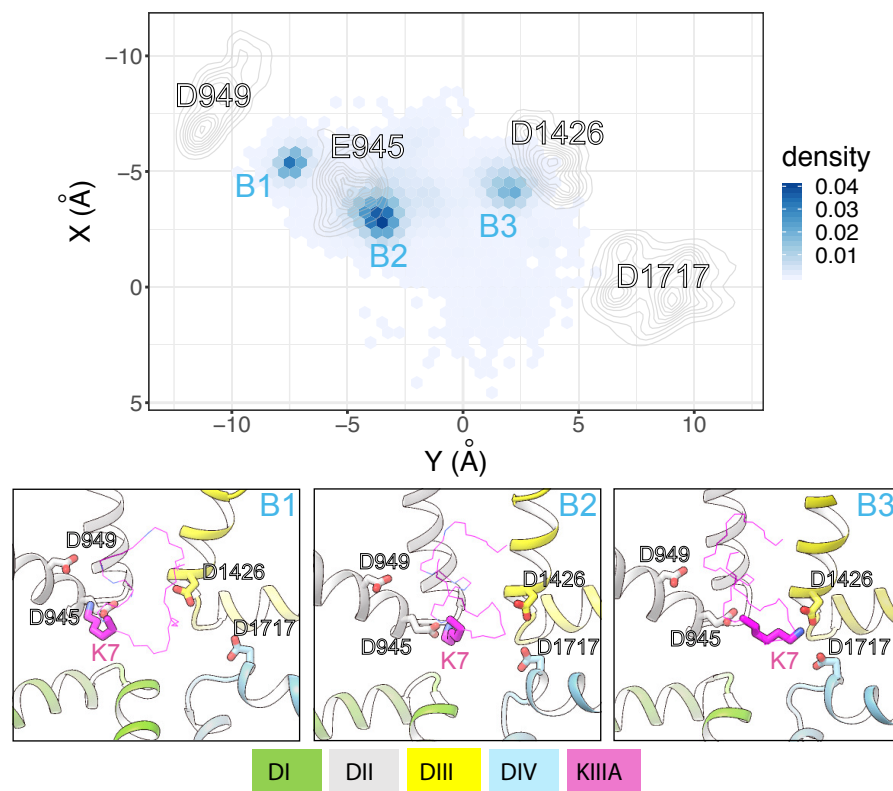


## Figure 5

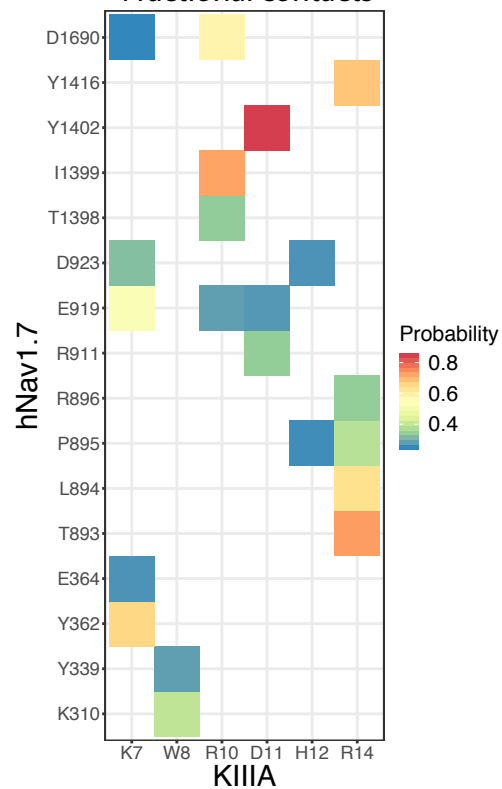
### A Coupling of K7 with acidic residues on hNav1.7 P2 helices



### B Coupling of K7 with acidic residues on hNav1.2 P2 helices



### C Fractional contacts



### D

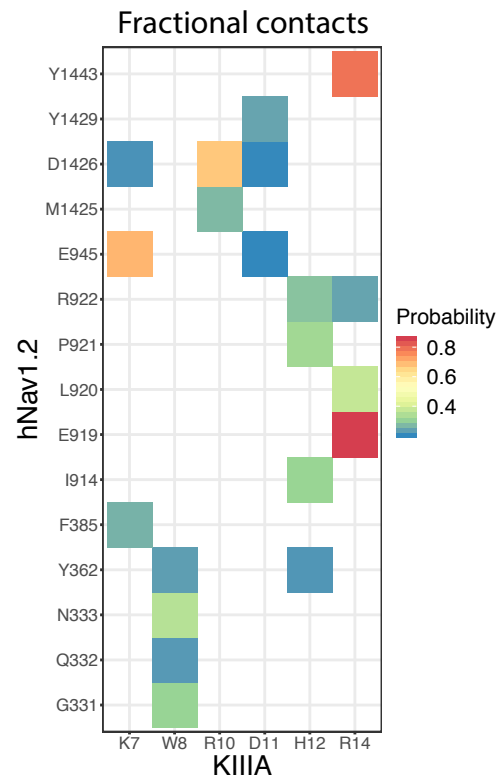
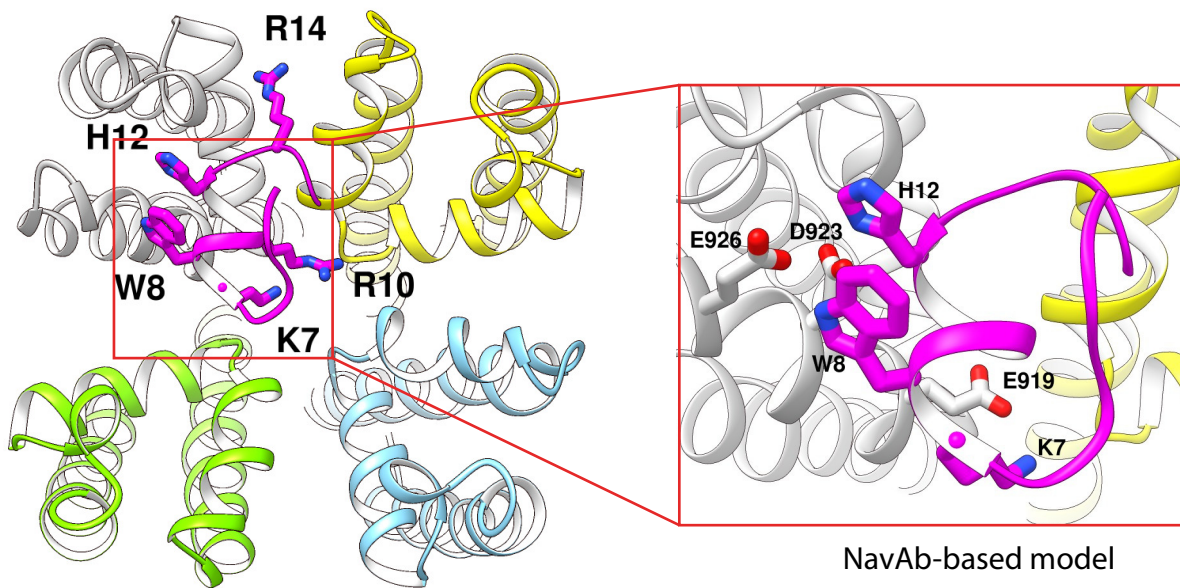


# Figure 1—figure supplement 1



A



B

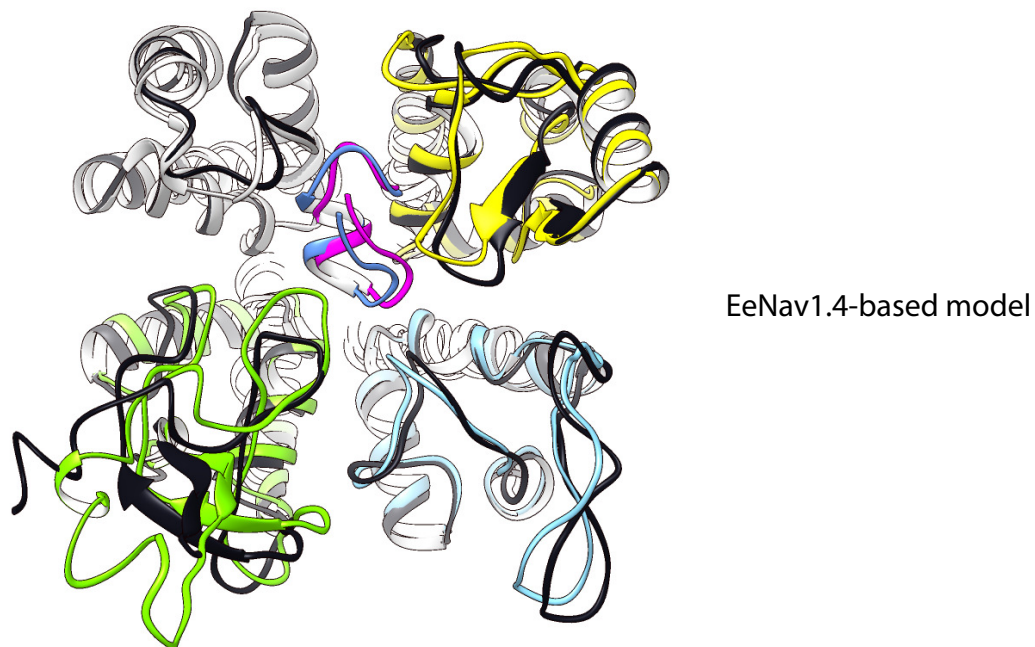


# Figure 2 - Figure supplement 1

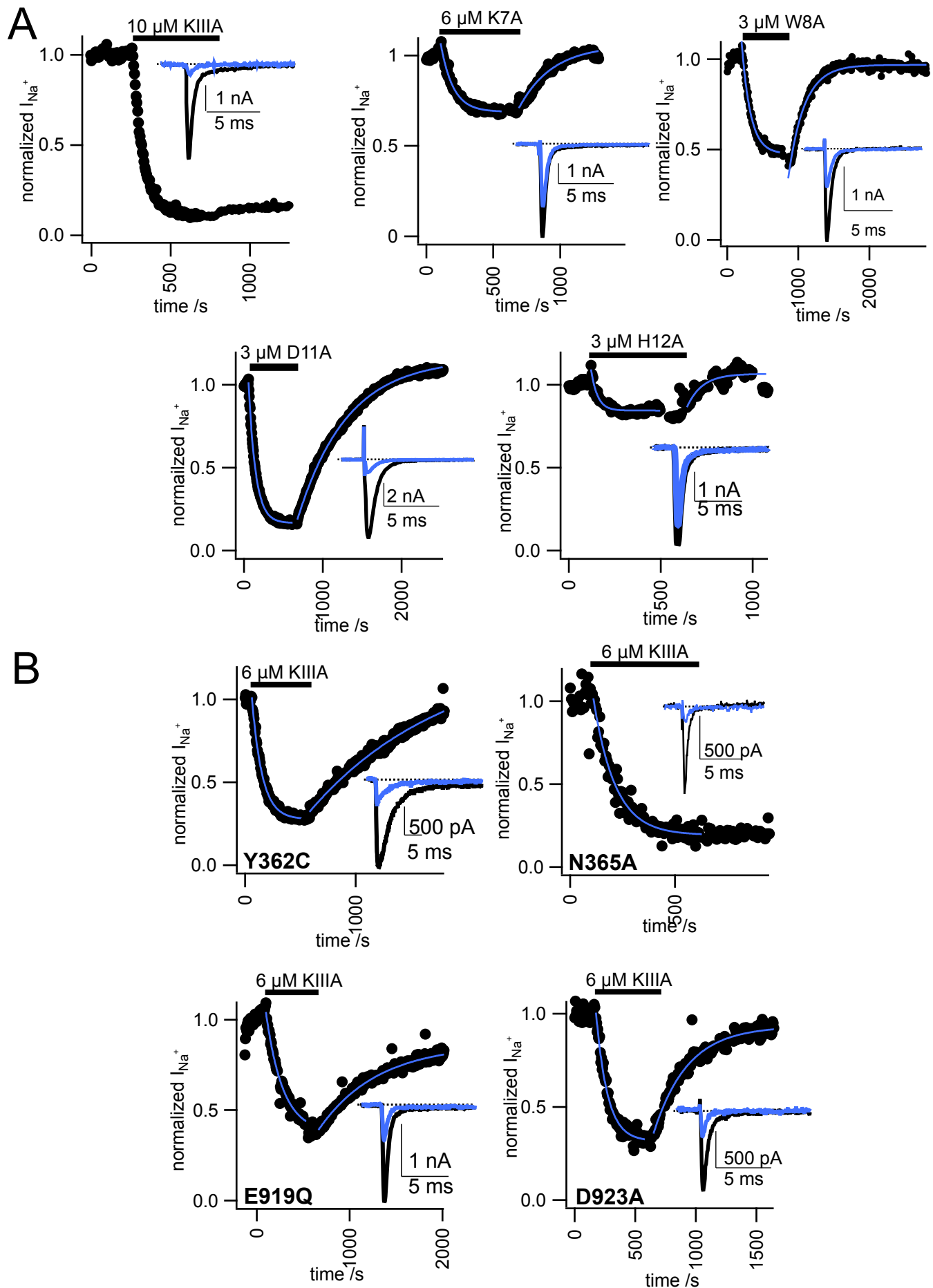




# Figure 3 - figure supplement 1

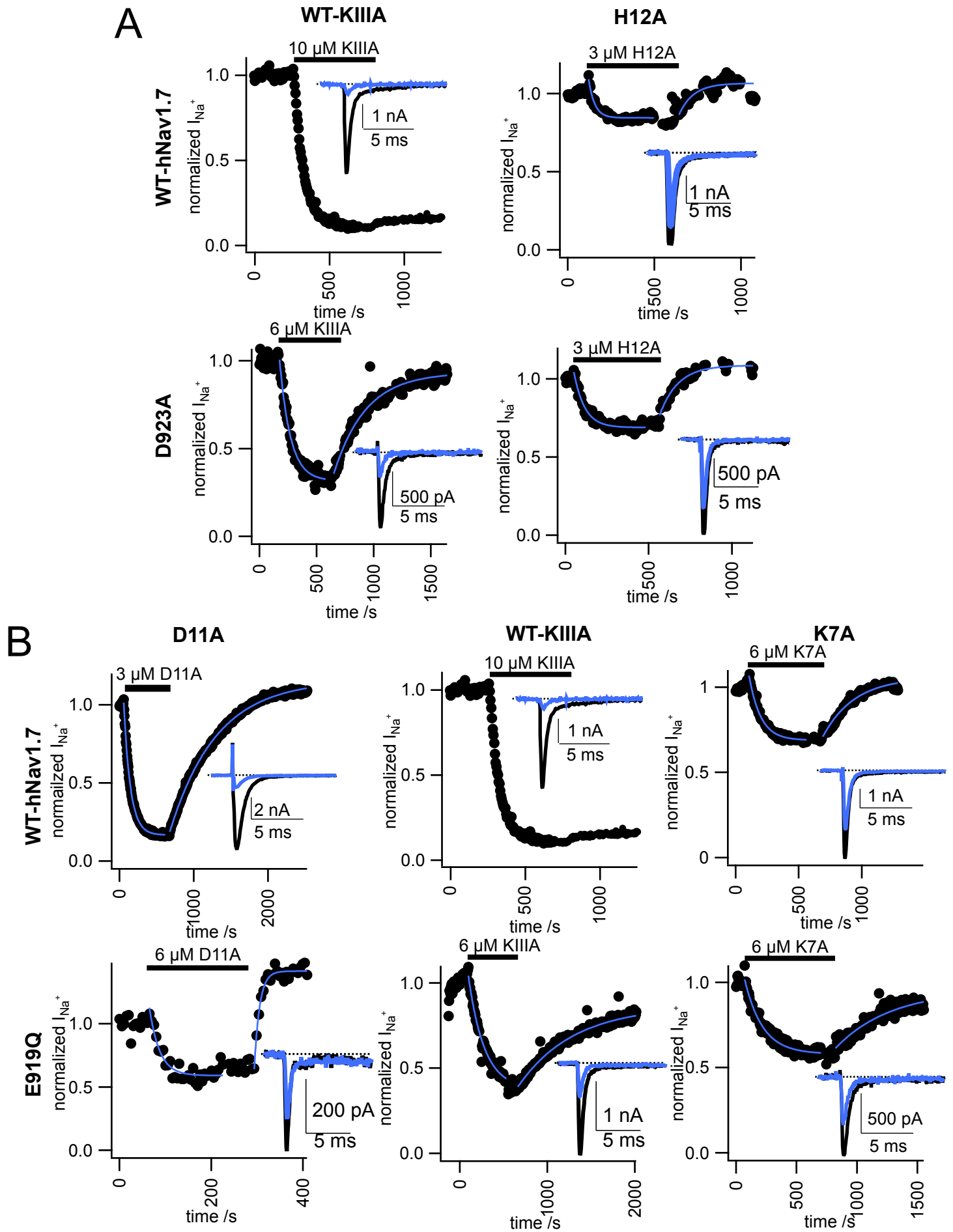


## Figure 4—figure supplement 1

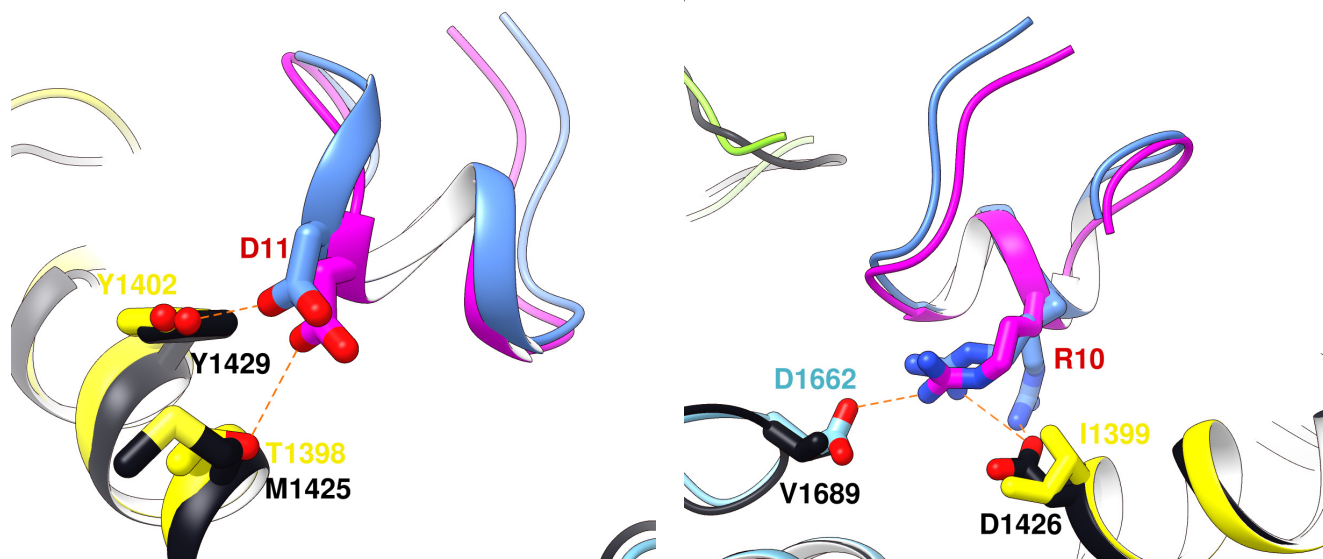
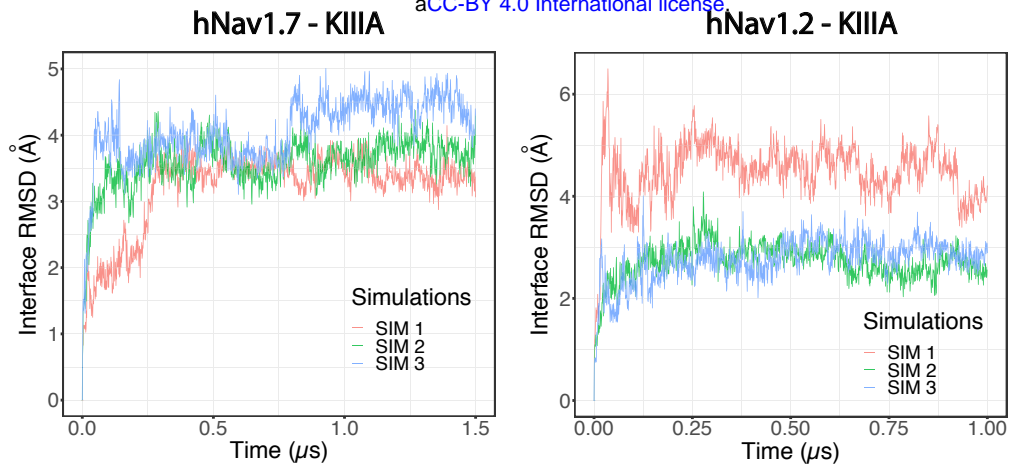


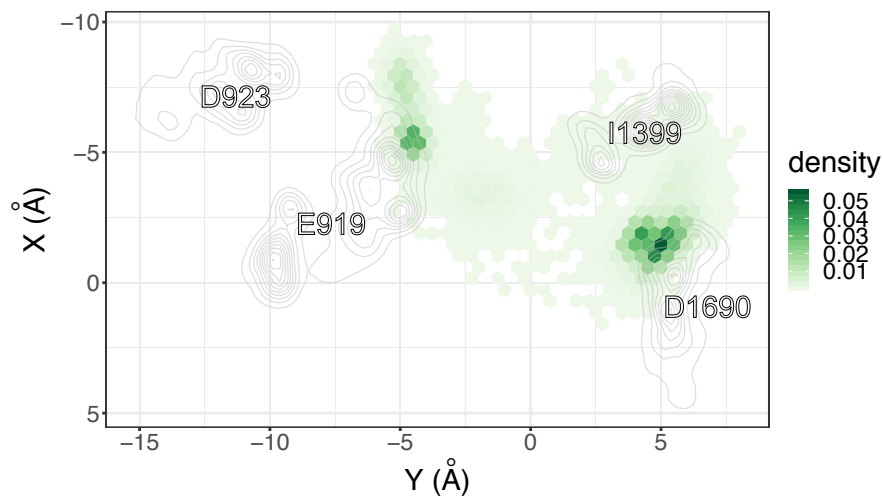
# Figure 5— figure supplement 1

**A** bioRxiv preprint doi: <https://doi.org/10.1101/654889>; this version posted May 20, 2021. The copyright holder for this preprint (which was not certified by peer review) is the author/funder, who has granted bioRxiv a license to display the preprint in perpetuity. It is made available under aCC-BY 4.0 International license.



**B**

Couplings of R10 with key acidic residues on hNav1.7 P2 helices



Couplings of R10 with key acidic residues on hNav1.2 P2 helices

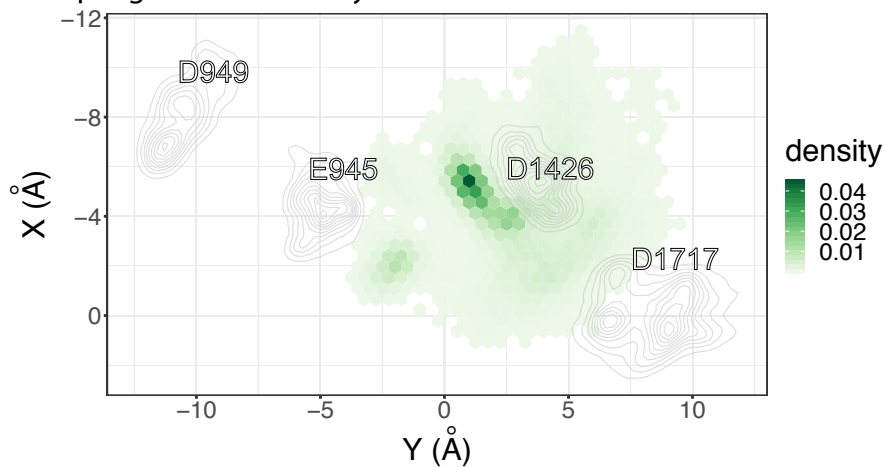




## Figure 5—figure supplement 2

### A Representative atomic contacts of K7 and R10 with acidic residues on P2 helix of hNav1.7

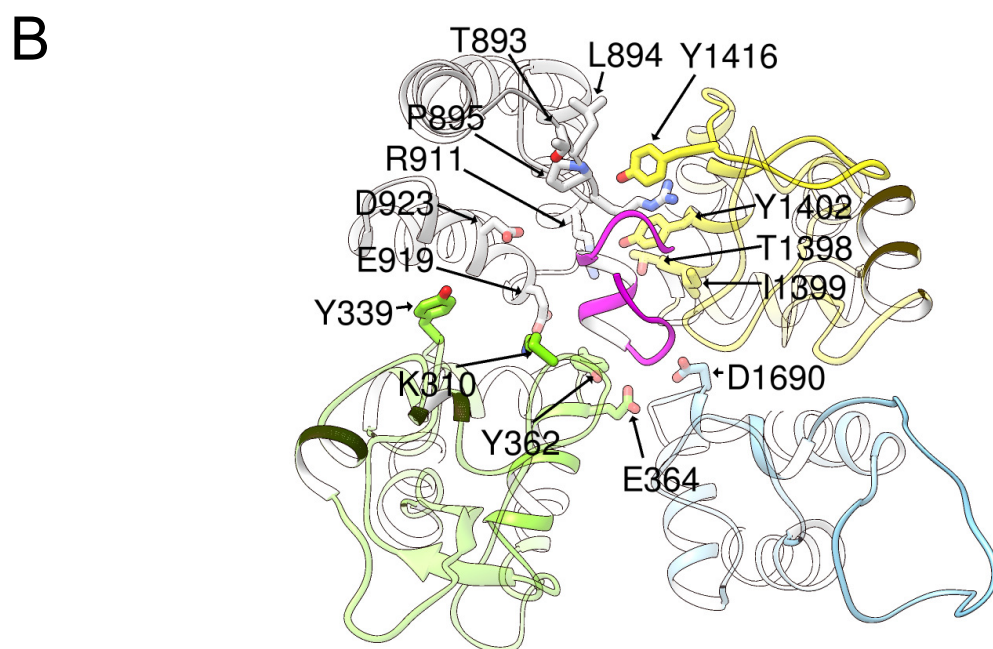
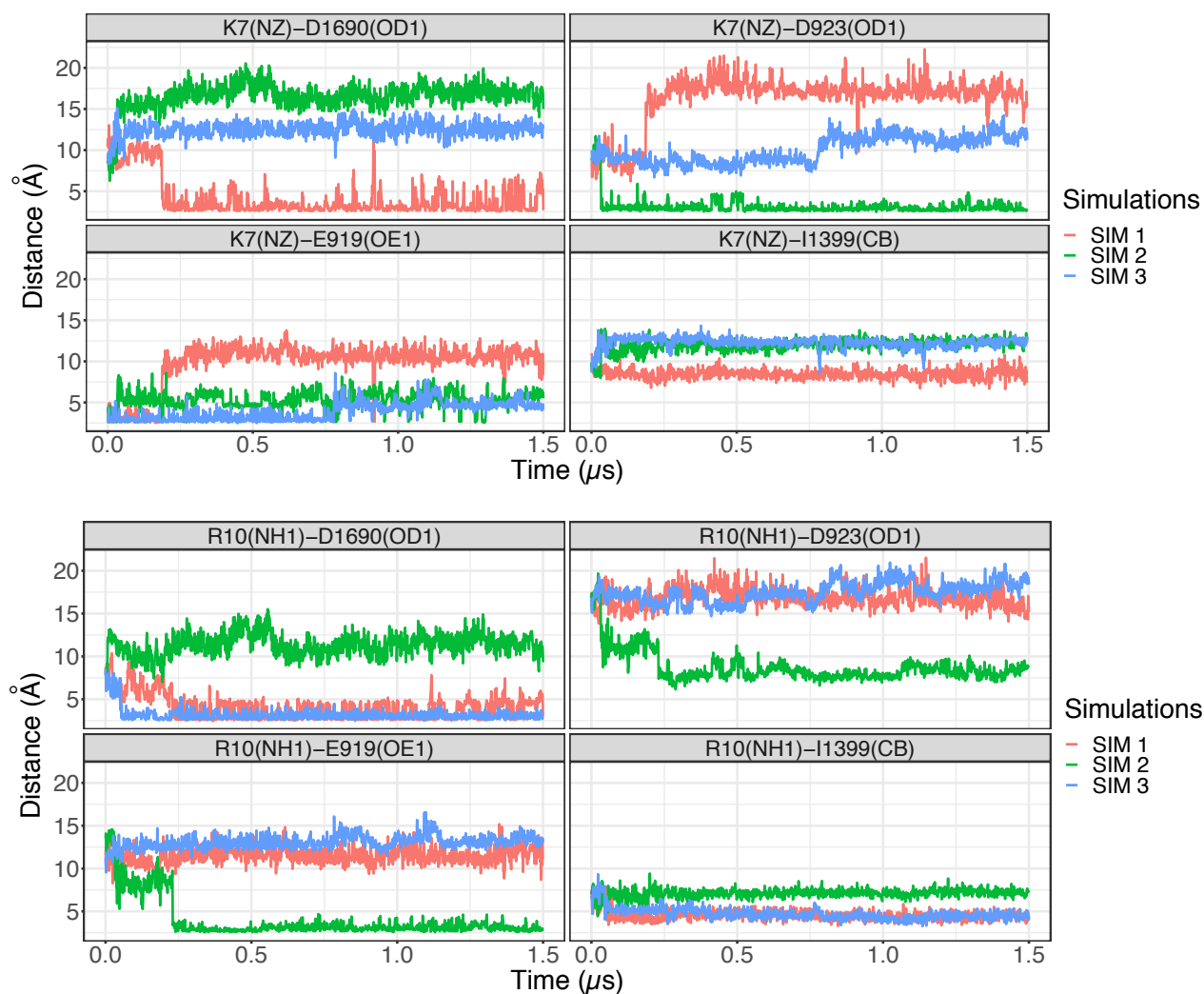
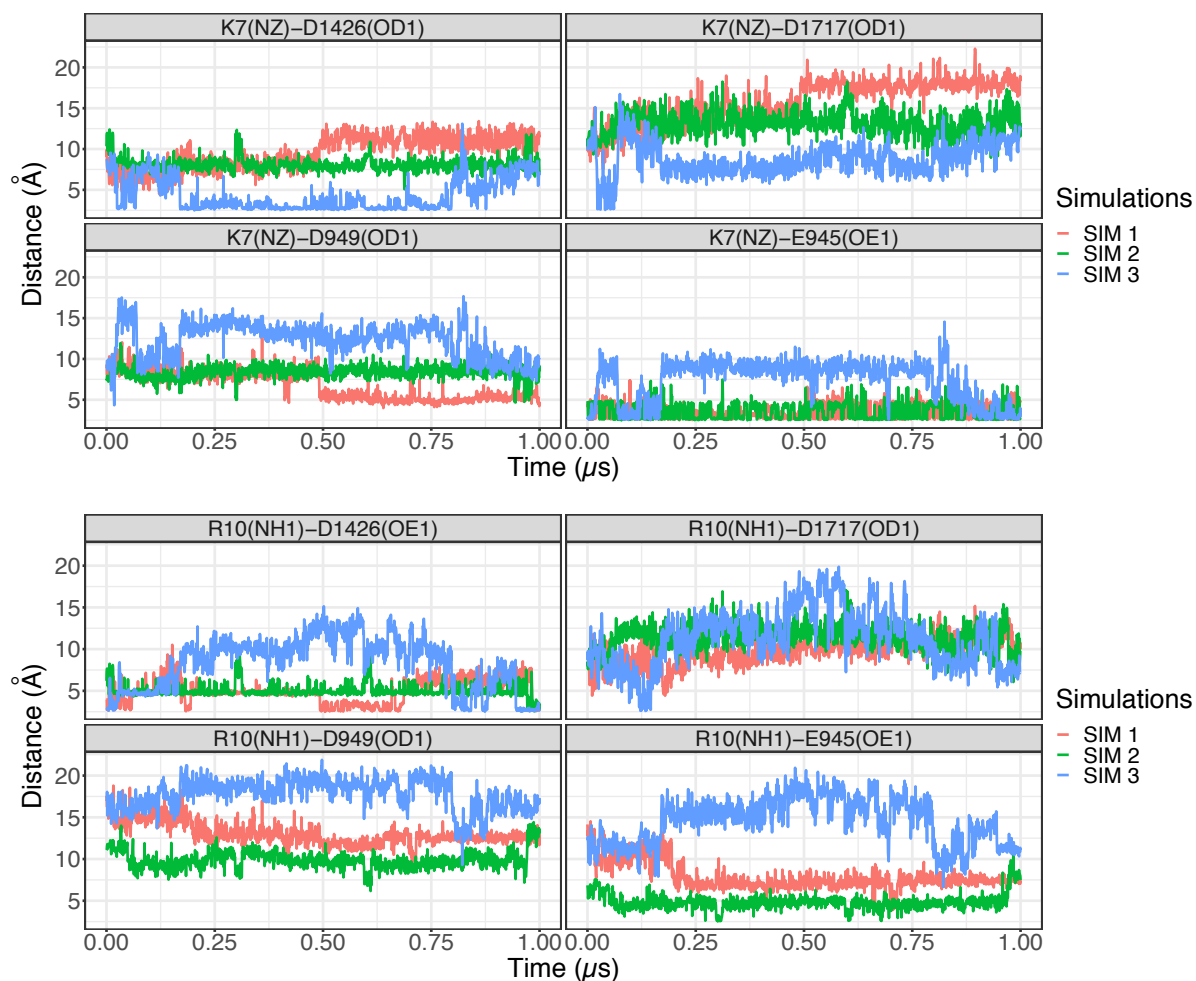


## Figure 5 figure supplement 3

### A

Representative atomic contacts of K7 and R10 with acidic residues on P2 helix of hNav1.2



### B

